Journal of Aircraft
Vol. 56, No. 5, September–October 2019

Hydrogen Fuel Cells and Batteries for Electric-Vertical Takeoff and Landing Aircraft

Wanyi Ng* and Anubhav Datta†
University of Maryland, College Park, Maryland 20742

DOI: 10.2514/1.C035218

The primary drawbacks of battery-powered vertical takeoff and landing [electric vertical takeoff and landing (eVTOL)] aircraft are their poor range and endurance with practical payloads. The objective of this paper is to examine the potential of hydrogen fuel cells to overcome this drawback. The paper develops steady-state and transient models of fuel cells and batteries, and it validates the models experimentally. It demonstrates fuel cell and battery power sharing in a regulated parallel configuration to achieve a reduction in powerplant weight. Finally, the paper outlines the weight models of motors, batteries, and fuel cells needed for eVTOL sizing, and it carries out a sizing analysis for on-demand urban air-taxi missions. This revealed that, for ranges within 75 miles, a lightweight (5000–6000 lb gross weight) all-electric tilting proprotor configuration is feasible with current levels of battery specific energy (150 $(\mathrm{W \cdot h})/\mathrm{kg}$) if high C-rate batteries are available (4–10 C for 2.5 min). For any mission beyond 50 miles, fuel cells appear to be a compelling candidate. Although fuel cells alone do not offer significant improvements to batteries, the two electric power sources can be combined for significant payload gains. In the combined powerplant, the fuel cell is sized to the low-power cruise mode and the battery supplements during higher power. For missions of less than 50 miles, the combination provides no advantage with current technology, and battery specific energy is the principal driver.

Nomenclature

A_c	=	fuel cell active area, m^2
ASR_Ω	=	fuel cell area specific resistance, $\Omega \cdot \mathrm{cm}^2$
a_A	=	fuel cell activation loss constant for anode
a_C	=	fuel cell activation loss constant for cathode
b_A	=	fuel cell activation loss constant for anode
b_C	=	fuel cell activation loss constant for cathode
C	=	concentration loss constant, V
C_{dl}	=	dielectric layer or double layer capacitance, F
E_r	=	ideal reversible voltage, V
F	=	Faraday's constant; 96, 485 C/mole
i	=	current density, $\mathrm{A/cm}^2$
I_{out}	=	current supplied by fuel stack or battery, A
i_{0A}	=	fuel cell activation loss constant for anode
i_{0C}	=	fuel cell activation loss constant for cathode
N_{units}	=	battery number of units in series
n_{cell}	=	battery or fuel cell number of cells
P	=	power supplied by the fuel stack, W
P_B	=	power supplied by the battery, W
P_C	=	power to cruise, W
P_H	=	power to hover, W
P_{kW}	=	power, kW
Q_{Nm}	=	torque, $\mathrm{N \cdot m}$
R	=	ideal gas constant, 8.314 $\mathrm{J/(mol \cdot K)}$
R_{ct}	=	charge transfer resistance, Ω
R_s	=	series resistance, Ω
t_c	=	fuel cell thickness, m
V_C	=	cruise speed, ft/s
V_{out}	=	voltage supplied by fuel stack or battery, V
v_c	=	cell voltage, V
v_{ss}	=	steady-state fuel cell voltage, V
$\dot{W}_F$	=	hydrogen flow rate, kg/s
W_{GTO}	=	gross takeoff weight, lb
W_{PAY}	=	payload weight, lb
w_f	=	hydrogen storage weight fraction
α_A	=	fuel cell activation loss constant for anode
α_C	=	fuel cell activation loss constant for cathode
ζ	=	battery maximum current rating (C rate), 1/h
η	=	battery charging efficiency
η_{act}	=	fuel cell activation loss
η_{conc}	=	concentration loss
η_{ohmic}	=	ohmic loss
ρ_c	=	fuel cell area density, $\mathrm{kg/m}^2$

I. Introduction

RECENT advances in electrochemical power and permanent magnet motors have caused a significant resurgence of interest in manned electric vertical takeoff and landing (eVTOL) aircraft [1,2]. We define eVTOL as vertical lift aircraft propelled by electric power and capable of carrying people. Since the world's first electric manned helicopter flight in 2011 [3] and the first multirotor helicopter flight in 2012 [4], developers ranging from startups to major aerospace corporations have introduced many eVTOL concepts in various stages of development. Electric power promises the potential for cleaner, quieter, safer, and more agile aircraft, which are essential characteristics for a new urban air mobility system. Cleanliness results from the lack of particulate pollution from the aircraft, often in densely populated areas, as well as the potential for renewable energy to charge batteries and power water electrolysis for hydrogen production for fuel stacks. Quietness results from a combination of reduced engine noise and slowed tip speeds enabled by electric motors and optimized for primarily forward flight missions. Safety results from redundancy in distributed proprotors and multiple power sources. Agility results from the ability to quickly vary rotor revolutions per minute and the increased thrust moment in distributed propulsion. In 2017, Uber released a vision for such a system in a white paper [5]. The principal drawback of these potential aircraft is the poor range and endurance with a practical payload (at least two passengers). This drawback stems from the weight of lithium–ion batteries. With the current state of the art, a practical aircraft cannot be flown. The objective of this paper is to examine the use of hydrogen fuel cells to overcome this drawback.

A major limitation for battery-powered eVTOL is the specific energy of lithium–ion batteries: 250 $(\mathrm{W \cdot h})/\mathrm{kg}$ for cells (Panasonic)

Presented as Paper 2018-1750 at the AIAA Science and Technology Forum, Orlando, FL, 8–12 January 2018; received 18 August 2018; revision received 31 January 2019; accepted for publication 6 March 2019; published online 18 September 2019.

*Graduate Research Assistant, Aerospace Engineering, Room No. 2140, Manufacturing Building. Student Member AIAA.

†Associate Professor, Aerospace Engineering, Room No. 3125, Glenn L. Martin Hall. Associate Fellow AIAA.

and 150–170 $(\mathrm{W \cdot h})/\mathrm{kg}$ for packs (Tesla, Saft). Proton exchange membrane (PEM) fuel cells can offer significantly higher specific energy than batteries in a unit that is still clean and hydrocarbon free, mechanically simple, operates at low temperatures (80–100°C), and produces no harmful emissions during flight. The limitation for fuel cells is lower power density: around 0.5 kW/kg (see, for example, the US Navy's Ion Tiger stack or the commercially available Hydrogen Energy Systems A1000 stack). A combination of the high specific power of batteries with the high specific energy of fuel cells can reduce the overall powerplant weight, allow fast charging and refueling, and introduce redundancy in the power source for added safety.

Fuel cell and battery hybrid systems have been demonstrated in all-electric manned fixed-wing aircraft. The Boeing Fuel Cell Demonstrator achieved manned flight in 2008 with a gross weight of 870 kg for approximately 45 min [6]. The German Aerospace Center's electric motor glider Antares DLR-H2 has been successfully used as a flying testbed with a gross takeoff weight of 825 kg [7–9]. The Polytechnic University of Turin developed a two-seater hybrid aircraft that achieved an endurance of 40 min [10]. These aircraft serve as a proof of concept for fuel-cell-powered flight.

However, all of the aforementioned are fixed-wing, and not rotary-wing, aircraft. eVTOL requires a rotary-wing aircraft, which has unique challenges associated with high hover power, low lift-to-drag ratios (due to the edgewise rotor and hub drag), and highly transient power profiles, including high power during both takeoff and landing. Recently, unmanned rotary-wing drones have been flown using fuel cells, but these are small-scale aircraft and scarce data are available in the public domain. These aircraft include the United Technologies Research Center's 1.75 kW, 10 kg, single main rotor helicopter in 2009 [11] and EnergyOr's 1.5 kW, 9.5 kg quadcopter in 2015 [12]. This paper deals with manned aircraft. The possible benefits of battery/fuel-cell (B-FC) hybridization for manned electric rotorcraft were reported for a R22 Beta II helicopter [13,14] in a conceptual study. This paper provides an actual demonstration of power sharing through hardware testing, and it carries out eVTOL sizing based on measured overhead and efficiency data. It summarizes the methodology and principal results of the work reported in Refs. [15,16].

The first step is to develop new propulsion system models for the design of this new class of aircraft. There have been several efforts in recent years to build such models [13,17–20] and apply them to the conceptual design of rotorcraft [14,21]. However, these models are all limited to steady-state operation. Models that can predict both steady state and transients would allow for refined sizing as well as an analysis of load transients and unsteady maneuvers of an aircraft. In this paper, batteries and fuel cells are modeled as equivalent circuit networks (ECNs) using resistor–capacitor models. The transient models predict voltage variation due to rapid changes in current. For batteries, they also capture the variation due to the state of charge. The models are calibrated (for time constants) and validated (for phenomenological trends) using an experimental setup. The setup consisted of a commercial fan-cooled proton exchange membrane fuel stack, pressurized hydrogen equipment, and a lithium–polymer battery connected in parallel to an electronic load as well as a flying quadrotor. A fuel cell requires many pieces of accessory equipment, called the balance of plant, that incur power losses and add weight overhead. The setup was also used to determine these balance-of-plant losses and overheads.

The second step, which is the sizing of eVTOL, begins with state-of-the-art data for motor and battery weights as the basis for weight models. A geometry- and material-based weight breakdown is used, which is guided by (in-house) measurements from a commercial fan-cooled low-power stack, as well as reported literature on the custom-built liquid-cooled high-power automobile stacks of Honda [22] and Toyota [23,24].

Sizing of the aircraft calculates the minimum gross (total) takeoff weight and payload weights that are achievable for a prescribed mission. The structural weights are based on simple expressions, correction factors, and available data on existing aircraft so that the primary focus remains on the impact of the new powerplant. The results are compared for different powerplant configurations: turboshaft, battery alone, fuel stack alone, and battery and fuel stack hybrid. They are also compared for edgewise and tilting proprotor configurations.

Specific targets are based on Uber's white paper [5] for a demonstration of sizing. The maximum installed power was taken to be 500 kW (hover) with cruise at the best range velocity. Details of the mission are provided in the aircraft sizing section (Sec. VI).

The effects of technology advances are investigated. The baseline results use parameters that are currently feasible at the component level. These parameters include battery specific energy, fuel stack specific power, and hydrogen tank weight fractions. Only the battery maximum current, or C rate, is allowed to vary beyond what is reported at this capacity level. Results are also calculated based on improved technology forecast for each individual component: for example, a battery specific energy of 250 $(\mathrm{W \cdot h})/\mathrm{kg}$ envisioned by the automobile industry; a fuel stack specific power of 2 kW/kg reported by Toyota; and a hydrogen weight fraction of 7.5%, which is a target met by the U.S. Department of Defense's hydrogen fuel cell program for pressured storage that is well within the 10% reported by the United Technologies Corporation (UTC) fuel cell helicopter. These technology assessments provide insights for prioritizing future investments.

The first part of the paper (Secs. II–IV) deals with hardware and model development. The second part (Secs. V and VI) deals with weights and aircraft sizing. The second part relies on the weights and efficiencies measured in the first part. The first part draws its motivation from the principal result of the second part, which is that a battery and fuel cell combination can be superior to either power source alone. Thermal effects are not modeled in the first part, but they are built into weights in the second part. Cost is ignored.

II. Experimental Setup

A commercial 300 W PEM fuel stack and a 2800 mAh 3 cell lithium–polymer battery were used to construct a simple testbed to understand the system overheads and acquire test data for calibrating and validating the fuel cell and battery models. Overheads include the balance of plant losses and accessory weights, which are later used for aircraft sizing. Due to the surrogate nature of the setup (non-flightworthy), these overheads are expected to be conservative. Figure 1 provides a basic flow diagram of how power is delivered in a parallel hybrid system from the battery and fuel stack to a load. This applies to the setup used in power sharing demonstrations described in Sec. IV. The unregulated version of power sharing architecture is a direct connection of the two power sources in parallel with diodes to ensure the current always flows away from the power source. The regulated version adds controlled charging and discharging of the battery in a strategic manner to minimize the powerplant weight. The data loggers record the current and voltage over time.

The fuel stack controller controls the supply and purge valves to allow hydrogen flow in and out of the fuel stack. This controller

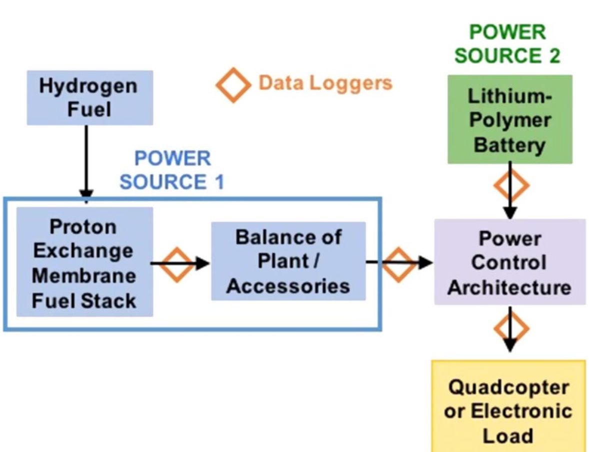

Fig. 1 Flow diagram of a parallel hybrid power system.

Table 1 Mass breakdown of experimental setup

	Component	Mass, g	Percent of total mass, %
Fuel stack	Fuel stack (300 W)	——	——
	Supply valve	——	——
	Purge valve	——	——
	Cooling fan	——	——
	Total	2901	44.6
	Controller	433	6.7
	Display	66	1
Balance of plant/accessories	Battery for controller	216	3.3
	dc–dc converter	943	14.5
	Data loggers (four)	158	2.4
	Displays (four)	54	0.8
	Cable stub, dc converter in	30	0.5
	Cable stub, dc converter out	28	0.4
Hydrogen system	Hydrogen regulator	840	12.9
	Hydrogen (35 L at 515 psig)	602	9.3
	Tube, hydrogen inlet	14	0.2
	Tube, purge	3	0.05
Total	——	6503	——

requires external power that can be provided by a power supply or an additional battery. The fuel stack operates at around 50 V, and so a dc–dc converter is used to reduce this voltage to that of the battery: to around 12 V. The power output from the fuel stack is connected in parallel with a battery. The combined power is then connected to a benchtop programmable electronic load for controlled tests. It is also connected to a quadcopter for tethered flight tests. A photograph of the hardware and a detailed plumbing and wiring diagram are available in Ref. [15].

To calibrate the fuel stack and battery model, it was necessary to isolate the power sources and connect them individually to the load. These configurations are described in Sec. V in relation to the specific calibration processes.

The component weights are presented in Table 1. From these weights, the overhead mass associated with the dc–dc converter (including cables) was calculated to be 15% of the total mass. This is the portion of the system mass that would not be included in the specific energy of a fuel cell. The mass overhead for the hydrogen regulator is 13%, but this can likely be reduced for a digital pressure gauge and aerospace grade regulator. Data collection devices accounted for 4% mass overhead. Only the dc–dc stepdown mass overhead is used in the sizing calculations later. This low-end commercial fuel stack has a specific power of 0.1 kW/kg based on the fuel stack plus controller weight.

Power losses occurred at the dc–dc converter, the diodes for power sharing, and the tether that delivered power to the load. Only the first is used in sizing later. The percent loss due to the dc–dc converter was found experimentally for a sweep of steady-state power levels with the controllable load to be an average of 25% [15]. This steady-state characterization was compared to transient conditions during a quadcopter flight, which showed a smaller loss (13%). A loss factor of 20% is used in the sizing calculations presented later, which is conservative because this is a low-grade dc–dc converter.

III. Modeling Electrochemical Power Supplies

A. Fuel Stack Steady-State Model

Powerplant sizing calculations require steady-state voltage versus current (i-v or polarization) curves. A steady-state model was developed based on a well-accepted description of the underlying electrochemical behavior of a fuel cell [25], which was extended to include empirical corrections for fuel cell temperature and humidity based on data from Refs. [26,27]. Then, transient operating characteristics were modeled using an equivalent circuit network. The ECN model captures the principal characteristics of transient dynamics [28–31] through a capacitative (first order) linear behavior. The circuit elements that determine the underlying time constants are calibrated using in-house experiments using the setup described earlier.

The steady-state behavior of the fuel stack is modeled using Eq. (1). The voltage $v(i)$ is a function of the current density i and is equal to the ideal or open circuit voltage E_r minus activation, ohmic, and concentration losses. It consists of eight empirically derived thermodynamic constants: $\alpha_A, \alpha_C, i_{0A}, i_{0C}$ (unitless constants), C (constant in volts), ASR_Ω (area specific resistance in ohms per square centimeter), i_L (limiting current in amperes per square centimeter), and i_{leak} (leakage current in amperes per square centimeter). The constant E_r can be predicted empirically or taken from test data:

$$
\begin{aligned}
v(i) &= E_r - \eta_{\mathrm{act}} - \eta_{\mathrm{ohmic}} - \eta_{\mathrm{conc}} \\
E_r &= 1.229 - (T - 298.15) \times 8.46 \times 10^{-4} + 4.309 \\
&\quad \times 10^{-5} (\ln p_{H_2} + 1/2 \ln p_{O_2})
\end{aligned}
\tag{1}
$$

for a pressure of 1 atm and the temperature T (in kelvins):

$$
\begin{aligned}
&\eta_{\mathrm{act}} = (a_A + b_A \ln(i + i_{\mathrm{leak}})) + (a_C + b_C \ln(i + i_{\mathrm{leak}})) \\
&\eta_{\mathrm{ohmic}} = i\mathrm{ASR}_\Omega \qquad \eta_{\mathrm{conc}} = C \ln \frac{i_L}{i_L - (i + i_{\mathrm{leak}})} \\
&a_A = -\frac{RT}{\alpha_A n_A F} \ln i_{0A} \qquad b_A = \frac{RT}{\alpha_A n_A F} \\
&a_C = -\frac{RT}{\alpha_C n_C F} \ln i_{0C} \qquad b_C = \frac{RT}{\alpha_C n_C F}
\end{aligned}
$$

The partial pressures are $p_{\mathrm{H}_2} = 1$ (pure hydrogen) and $p_{\mathrm{O}_2} = 0.21$ (partial pressure of oxygen in air).

Figure 2 summarizes the state of the art in fuel cell (FC) performance. Data measured from the fuel stack used in this paper are represented as “FC-1 data-1.” “FC-1 data-2” are the manufacturer’s specifications. They are close, as expected. Two other datasets are shown for comparison. FC-2 is from a state-of-the-art (2015) Ref. [9] aerospace-grade stack similar to that used by the DLR, German Aerospace Center. FC-3 is from a state-of-the-art (2006) single cell reported in Ref. [26] at 1 atm and 80°C. The power density in Fig. 2b is simply the product of the cell voltage and current density shown in Fig. 2a. The fitted models are shown as lines: each with a different set of thermodynamic constants. The main difference is the high current and power from higher-quality cells. The next section on transients uses the constants for the present stack (FC-1 data-1), where $\alpha_A = 1.1$, $\alpha_C = 0.18$, $i_{0A} = 3\mathrm{e}-4$, $i_{0C} = 1\mathrm{e}-4$, $i_L = 0.31$, $i_{\mathrm{leak}} = 0.005$, $C = 0.01$, and $\mathrm{ASR}_\Omega = 0.2$. In the sizing section (Sec. VI), the polarization curve of FC-3 will be used, which is well within what is achievable for an aerospace fuel stack. For this stack, $\alpha_A = 1.1$, $\alpha_C = 0.15$, $i_{0A} = 0.1$, $i_{0C} = 1\mathrm{e}-4$, $i_L = 0.85$, $i_{\mathrm{leak}} = 0.01$, $C = 0.15$, and $\mathrm{ASR}_\Omega = 0.07$.

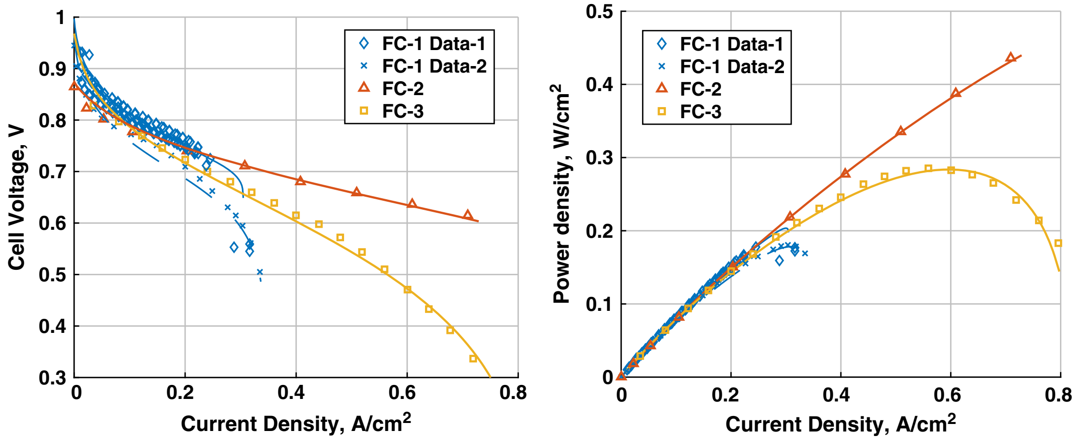

a) Cell voltage versus current density

b) Power density versus current density

Fig. 2 Steady-state characteristics of three different fuel cells (FC-1 through FC-3 defined in text): data and models.

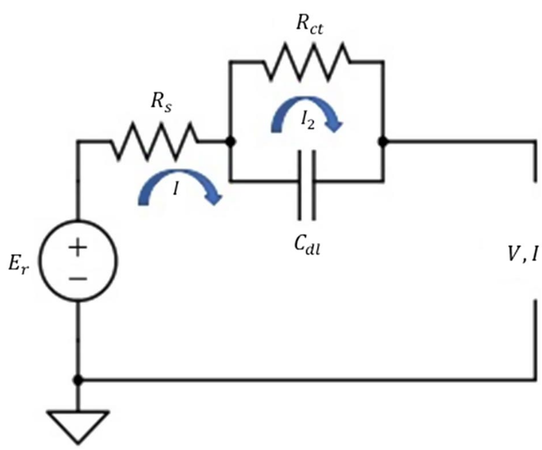

Fig. 3 Basic equivalent circuit network of fuel cell.

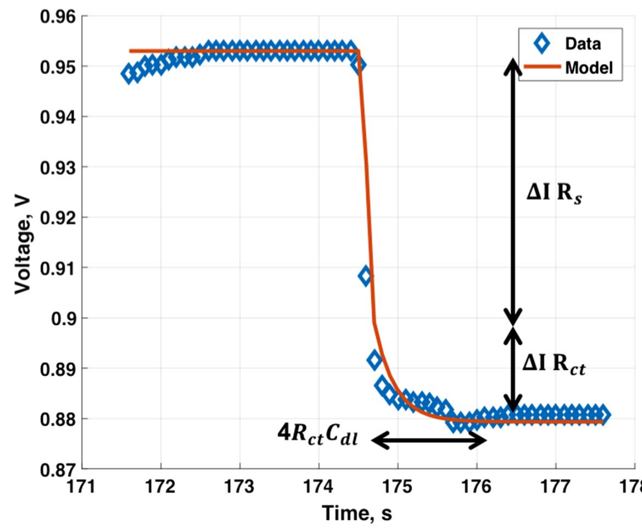

Fig. 4 Voltage response to a step current drawn from a fuel stack.

At a given pressure (here, 1 atm) the steady-state characteristics depend mainly on the temperature, the cathode relative humidity (CRH), and the anode relative humidity (ARH). Cell-level data obtained from Ref. [26] were used to find the variation of the thermodynamic constants of the model with temperature and humidity. The results can be found in Ref. [15]. The sizing section (Sec. VI) assumes a fuel stack temperature of 80°C, a CRH of 100%, and an ARH of 100%.

B. Fuel Stack Transients

To model the transients, an ECN for a single polarization model was used, as shown in Fig. 3. E_r is the open circuit voltage. V and I are the voltage and current output by the fuel cell, respectively, where I is now a function of time. R_s is the electrolyte resistance (ohmic resistance in steady state), and R_{ct} is the charge transfer resistance causing a voltage drop across the electrode–electrolyte interface (activation and concentration losses in steady state). C_{dl} is the dielectric or double-layer capacitance, which accounts for the transients and models the effects of charge buildup in the electrolyte at the anode–electrolyte or cathode–electrolyte junctions.

The voltage V for current I is given by

$$\begin{aligned} V &= E_r - R_s I - R_{\mathrm{ct}} I_2 \\ &= E_r - (R_s + R_{\mathrm{ct}})I + R_{\mathrm{ct}}(I - I_2) \\ &= v_{\mathrm{ss}} + R_{\mathrm{ct}}(I - I_2) \end{aligned} \tag{2}$$

where I_2 is found from the derivative of the voltage balance around the smaller loop:

$$R_{\mathrm{ct}} C_{\mathrm{dl}} \dot{I}_2 + I_2 = I \tag{3}$$

A more detailed derivation is available in Ref. [15].

Here, $v_{\mathrm{ss}} = E_r - (R_s + R_{\mathrm{ct}})I$ is the steady-state cell voltage corresponding to Fig. 2. This transient model collapses to a steady state when $\dot{I}_2 = 0$ and $I_2 = I$ (then, $V = v_{\mathrm{ss}}$). The values of the circuit components R_{ct} and C_{dl} were determined empirically. This was achieved by connecting the fuel stack output directly to an electronic programmable load. A step current was drawn from the fuel stack, and the transient voltage response was recorded. A sample of these data along with the empirically calibrated constants for two different current levels are given in Fig. 4 and Table 2. As depicted in Fig. 4, the magnitude of the transient is R_{ct} times the size of the current step ΔI, and the time for the voltage to achieve steady state is approximately 4τ, where $\tau = R_{\mathrm{ct}} C_{\mathrm{dl}}$ is the time constant. For the response to a step input, the model is given by the following equation, where t is the time after the step change and ΔI is the magnitude of the step change:

Table 2 Fuel cell ECN components calibrated for different current ranges

	Low current	Nominal current
Current density, A/cm^2	0.01–0.04	0.07–0.18
R_s, $\Omega \cdot$ cm^2	2.57	0.60
R_{ct}, $\Omega \cdot$ cm^2	1.22	0.09
C_{dl}, F	0.23	0.26
Time constant, s	0.28	0.023

$$V = E_r - \Delta I R_s - \Delta I R_{\mathrm{ct}}(1 - e^{-t/\tau}) \tag{4}$$

The values of R_s, R_{ct}, and C_{dl} were found to depend on the magnitude of the current. They were calibrated separately for a very low current and a nominal current, as shown in Table 2. The resistor values are much lower at the nominal current, which indicates that the transients are of smaller magnitude and duration than at low current.

C. Battery Steady-State Model

In a battery, the open circuit voltage E_r is no longer constant (like it is in the fuel cell), but it is instead a function of the battery's state of charge (SOC). The SOC describes the fraction of charge remaining in the battery over the total charge C (in ampere hours) possible for supply. In its simplest form, it is given by Eq. (5), where I is the current drawn in amperes, and t is the time in hours:

For discharge:

$$\mathrm{SOC} = 1 - \frac{1}{C}\int I\,\mathrm{d}t \tag{5}$$

For charge:

$$= \frac{1}{C}\int I\,\mathrm{d}t$$

However, C itself can be a function of I, and so this equation is hard to apply when the current changes with time. Typically, for Li–ion batteries, $C = C_{\mathrm{REF}}/\alpha\beta$, where C_{REF} is the capacity at a reference current I_{REF}, and $\alpha(I)$ and $\beta(T)$ are rate factors associated with other currents and temperatures. Then, a more appropriate expression for the SOC is as follows:

For discharge:

$$\mathrm{SOC} = 1 - \frac{1}{C_{\mathrm{REF}}}\int \alpha\beta I\,\mathrm{d}t \tag{6}$$

For charge:

$$= \frac{1}{C_{\mathrm{REF}}}\int \alpha\beta I\,\mathrm{d}t$$

The rate factors α and β have to be determined empirically. The quantity Idt is the actual amount of charge supplied or delivered to the load; the quantity $\alpha\beta Idt$ is a notional amount of charge released or depleted from the battery with which the state of charge is to be calculated.

A representative set of rate factors based on Ref. [32] are

$$\begin{aligned} \alpha(I) &= 1 + 0.4\left(\frac{I}{I_{\mathrm{REF}}} - 1\right)\frac{I_{\mathrm{REF}}}{C_{\mathrm{REF}}} \\ \beta(T^\circ C) &= 1 - 0.02093(T - T_{\mathrm{REF}}), \qquad \text{where } T_{\mathrm{REF}} = 23 \end{aligned} \tag{7}$$

The temperature also reduces the open circuit voltage (at all SOCs):

$$\Delta E_r = 0.011364(T - T_{\mathrm{REF}}) \tag{8}$$

The variation in E_r with the SOC means there is not a unique steady-state I–V curve as with the fuel stack. As the current is drawn, the SOC and E_r drop. This effect must be modeled. A fully empirical model based on the classical work of Shepherd [33] is adopted. For a constant current draw per unit area i, the Shepherd model has the following form:

$$\upsilon = E_r - iN \tag{9}$$

where

$$E_r = E_s - \frac{K}{\mathrm{SOC}}\, i + A\exp[-B(1 - \mathrm{SOC})] \tag{10}$$

E_r is the open circuit voltage, and υ is the battery output voltage. E_s is a constant potential in volts, K is a polarization coefficient in the Ω area, N is the internal resistance times the unit area in the Ω area, and A (in volts) and B (unitless) are empirical constants. The SOC here is the area specific state of charge. The original Shepherd model uses the SOC from Eq. (5) (and uses area specific capacity Q instead of capacity C); if α and β are available, Eq. (6) should be used instead. In total, four empirical constants (E_s, K, A, and B) describe the open circuit voltage E_r as a function of the SOC, and the additional constant N is the resistance needed for closed circuit voltage υ.

To calibrate the model for E_r, the battery was connected directly to a battery analyzer, which discharged the battery at a very low constant i and measured υ. The unit area was defined as the area of the cell, and so the current density (current per unit area) is equivalent to the total current drawn from the battery. N was taken to be the summation of R_s and R_{ct}, which are the internal resistances of the battery, which were calibrated using the same method described in Sec. III.B for the fuel stack (by drawing a step current and recording the resulting voltage). The remaining values were calibrated empirically based on the discharge data.

The discharge data are shown in Figs. 5 and 6 for a 30 C, 2800 mAh, three-cell lithium–ion battery. Figure 5 uses a model based on the six empirical constants extracted from the 0.07 C discharge data (lowest current), and it shows how the model performs at higher currents. Figure 6 uses empirical constants extracted from the 3.6 C discharge data (highest current) and shows how the model performs at lower currents. The main cause of this discrepancy at high currents is the change in K with current that is obvious from Fig. 6, which shows how the model performs when the constants are extracted using data from 3.6 C. Here, the discrepancy is shifted to low currents. None of this is surprising; even though the Shepherd constants have some basis in underlying phenomena, empirical models are always inadequate as prediction models: at best, the constants can be evaluated for several current levels, as shown in Table 3. The resistance N was extracted from step input experimental data, and it is equivalent to $R_s + R_{\mathrm{ct}}$ of the battery from Table 4, to be presented later. The capacity C was extracted by fitting the constant current discharge data. This value is consistent with the discharge capacity measured for each test by multiplying the current and the duration of discharge. It is slightly lower than the empirically fit capacity C because the discharge was stopped when the battery voltage reached 9 V to avoid damaging the battery. Most of the constants vary with the operating current. In this table, "area" refers to the same unit of area as that in the "current per area" i.

D. Battery Transient

The transient behavior of a battery can be modeled by the same equivalent circuit network as the fuel cell, because both are dc electrochemical sources. However, the open circuit voltage E_r is now a function of the state of charge. Many transient lithium–ion battery ECN models have been developed in the past two decades for the design of power systems in consumer electronics (see Refs. [32,34] for example) and hybrid-electric cars (see Ref. [35]). All of these models are semiempirical and require extensive battery testing for temperature and frequency effects. The E_r(SOC) would also have to be input separately as a function of temperature for all models.

The Shepherd model for E_r(SOC) is retained to capture the nonlinear behavior of the steady state and paired with an ECN model to capture the generally linear behavior of the transients. The transient model uses the same circuit diagram shown earlier in Fig. 3. The constants R_s, R_{ct}, and C_{dl} are extracted using the same method as the fuel stack. The results for low and nominal current ranges are presented in Table 4.

Although the capacitor values are larger as compared to the fuel stack, the resistor values are smaller. This manifests as voltage

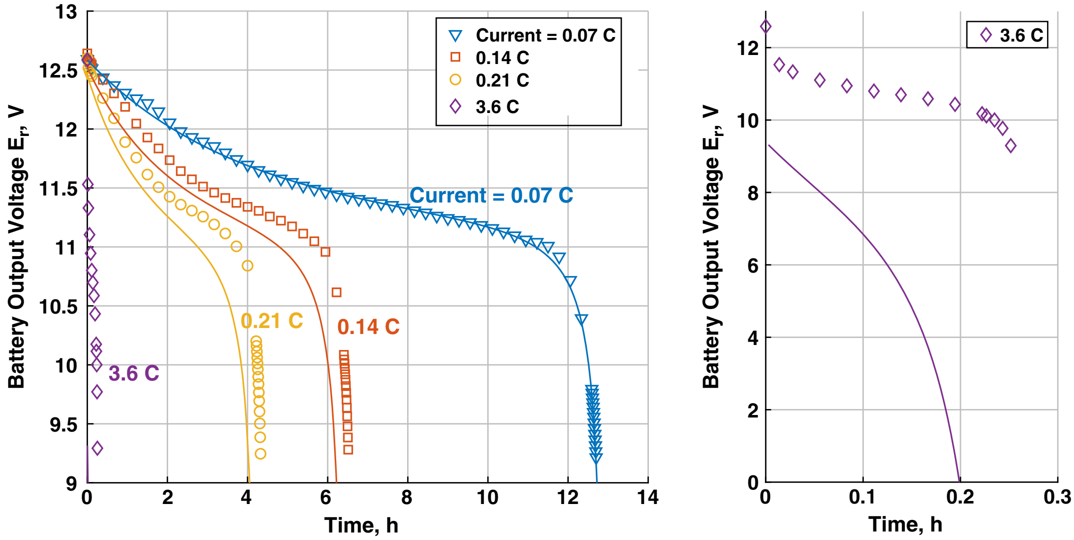

a) Discharge model compared to experimental data b) Close-up view of small time range

Fig. 5 Shepherd model compared to test data; model parameters extracted at 0.07 C.

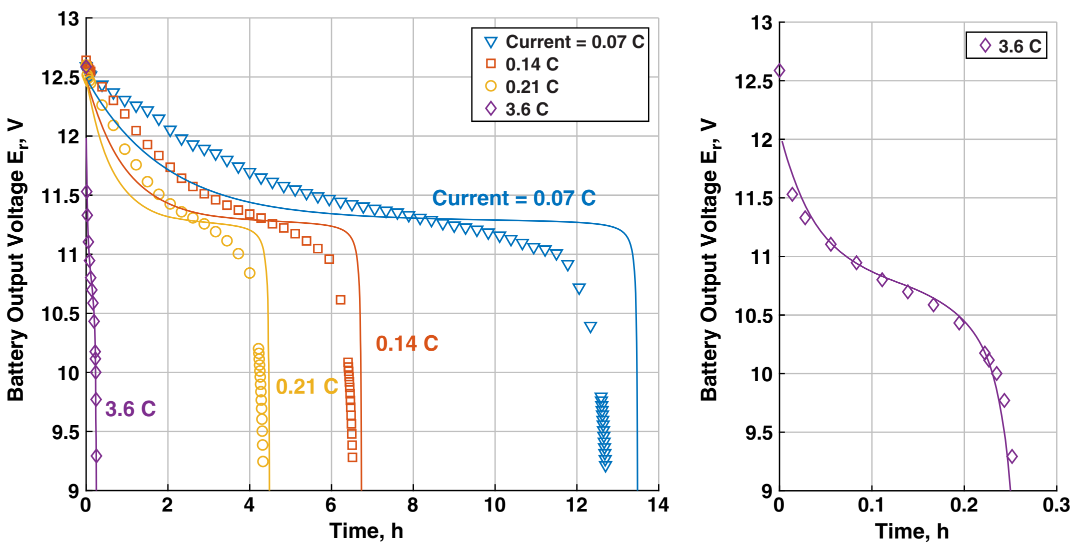

a) Discharge model compared to experimental data b) Close-up view of small time range

Fig. 6 Shepherd model compared to test data; model parameters extracted at 3.6 C.

transients of a lower magnitude but a longer settling time as compared to the fuel stack. The time constant of the battery is approximately one order of magnitude larger than that of the fuel stack.

E. Model Verification

For lithium–ion batteries and PEM fuel stacks to be used in eVTOL, they must be able to respond to rapid transients caused by maneuvers or electrical faults. Experimental data were acquired to verify the models in the presence of these rapid transients.

Figure 7 shows fuel cell voltage (measured for the stack and divided by the total number of cells) with intentionally high-amplitude and -frequency transients. The results indicate that the model is generally capable of capturing the transient I–V characteristics. A small vertical shift is visible between the model and the experimental voltage, which can be attributed to a measurement error or variations in the temperature and humidity between the time of this test and the time of the steady-state model calibration [used to find v_{ss} in Eq. (2)]. The primary error in the model

Table 3 Shepherd battery model constants for 2800 mAh, 30 C, 3 cell lithium polymer battery

	Very low current	Low current	Nominal operating current
Discharge current, A	0.2	0.4-0.6	10
Discharge C rate, h^{-1}	0.07	0.14	3.6
Discharge capacity, Ah	2.54	2.61	2.54
E_s, V	11.3	11.3	11.3
K, Ω area	0.25	0.1	0.015
Q, Ah/area	2.6	2.65	2.7
N, Ω area	0.076	0.076	0.028
A, V	1.35	1.35	1.2
B	3.4	3.4	7.0

Table 4 Battery ECN components calibrated for different current ranges

	Low current	Nominal current
Current, A	0.01–2.4	9.3–13.5
C rate, h^{-1}	0.0036–0.86	3.32–4.82
R_s, Ω	0.042	0.021
R_{ct}, Ω	0.034	0.007
C_{dl}, F	268.15	242
Time constant, s	9.12	1.69

occurs at the beginning of the test, which appears as a longer transient behavior that occurs upon startup of the fuel stack, which is not captured by the present model.

The transient model is compared to the steady state in Fig. 7b. This steady-state model is based on the FC-1 data-1 model in Fig. 2a. This comparison reveals the first major conclusion: the transient model is almost identical to the steady-state model. The steady-state model is capable of capturing almost all of the behavior in the normal range of operating currents, and so the transients in the fuel stack are not very significant. This is a reflection of the fact that the values of R_{ct} and C_{dl} in Table 2 are fairly small for the normal operating current range. The error at the beginning of the test duration is perhaps due to a second, larger internal capacitance not captured by the ECN used in this model.

Similar data were collected for the lithium–ion battery (Fig. 8). The model in this figure uses the empirical constants from the third set presented in Table 3. All three sets of constants were investigated and showed very small differences of less than 0.15 V. A comparison revealed the second key conclusion: unlike the fuel stack, here, the transient model is slightly different from the steady-state model and, in general, provides an improved waveform. However, like in the fuel stack, there is again a vertical shift between the model and the experimental voltage. The experimental voltage is lower, and so it cannot be due to heating (rise in temperature increases voltage), but it is perhaps due to rate effects at higher currents (higher current reduces voltage), which are not included in the model ($\alpha = 1$ in the model). Additionally, discrepancies could be due to the battery's total capacity degrading over use; the constant voltage discharge data used to calibrate the model were collected after the transient experiment, and the battery's capacity had reduced from a nominal 2.8 Ah to a lower 2.6 Ah.

The key conclusions from this transient modeling are that transients are not critical for powerplant sizing at the conceptual design stage, and that the fuel stack has, in fact, a faster response than the battery.

IV. Demonstration of Power Sharing

A. Unregulated

The battery and fuel stack are connected in parallel and used to power a tethered quadcopter. The data from each power source and the quadcopter load are shown in Fig. 9. The flight test demonstrates the viability of using the two power sources together in a hybrid powerplant. The architecture for the unregulated system is trivial; the two components are connected in parallel with only a diode in series with the fuel stack and a dc-to-dc converter, which is the same arrangement shown earlier in Fig. 1. The power flow is not regulated at all; the two components are left to operate based solely on their natural i-v characteristics. The key conclusion from Fig. 9 is that they form a natural combination working in tandem; the battery voltage drops with a depleting SOC, diminishing its share of power. This causes the fuel cell voltage to also drop, increasing its share of power (Fig. 2). Thus, the total power supply is maintained. Regulation would be required to force them not to work in tandem but instead share the supply of power as desired. This is an essential requirement for eVTOL, where the fuel stack is sized to low-power cruise mode and the battery supplements during high-power segments of the mission to minimize powerplant weight.

B. Regulated

A regulated system would conserve battery energy and use hydrogen energy whenever possible because hydrogen energy is more weight efficient. The battery would only be used during high-power portions of the mission to supplement the fuel stack. Additionally, if the battery is depleted, the excess power from the fuel stack can be used to recharge the battery. This is illustrated in Fig. 10.

In the regulated case, the battery no longer discharges during the low-power phases: spinup, transition, cruise, and spindown. Thus, less energy is drawn from the battery and more from the fuel stack. The regulated power sharing strategy reduces the total weight of the powerplant because batteries suffer from low specific energy but can provide higher specific power. Additional power would need to be incorporated to provide redundancy for failure of a battery or fuel stack.

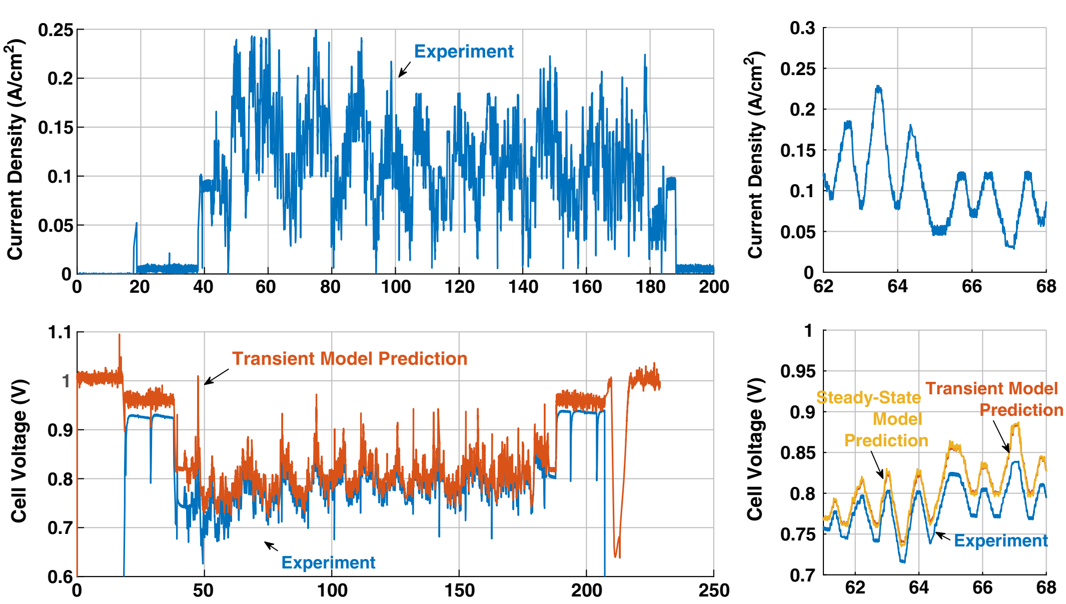

a) Full test duration

b) Close-up comparing steady-state and transient models

Fig. 7 Model compared to experimental voltage for fuel stack for highly transient load.

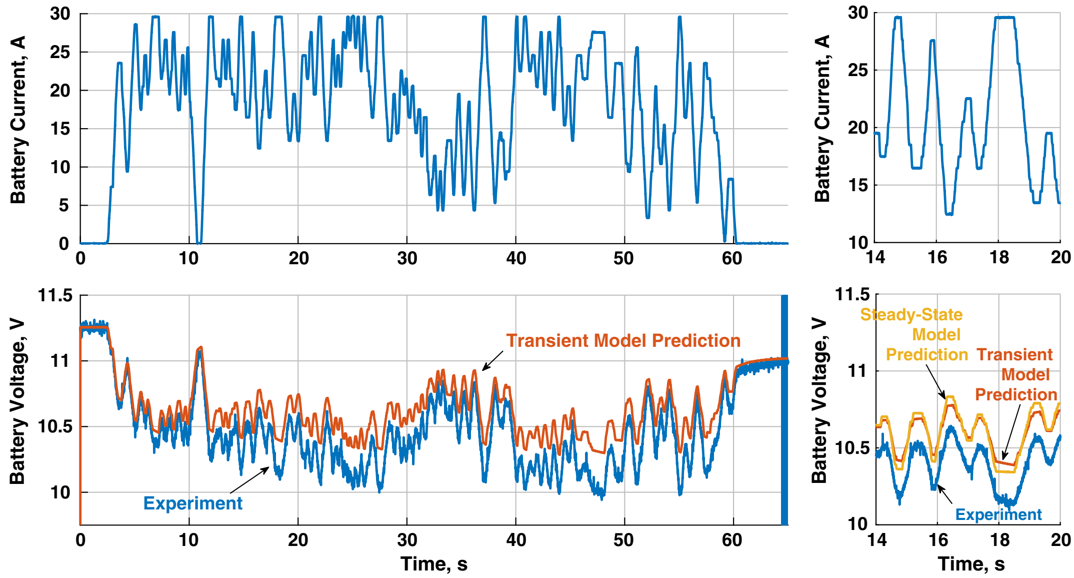

a) Full test duration

b) Close-up view comparing steady-state and transient models

Fig. 8 Model compared to experimental voltage for battery for highly transient load.

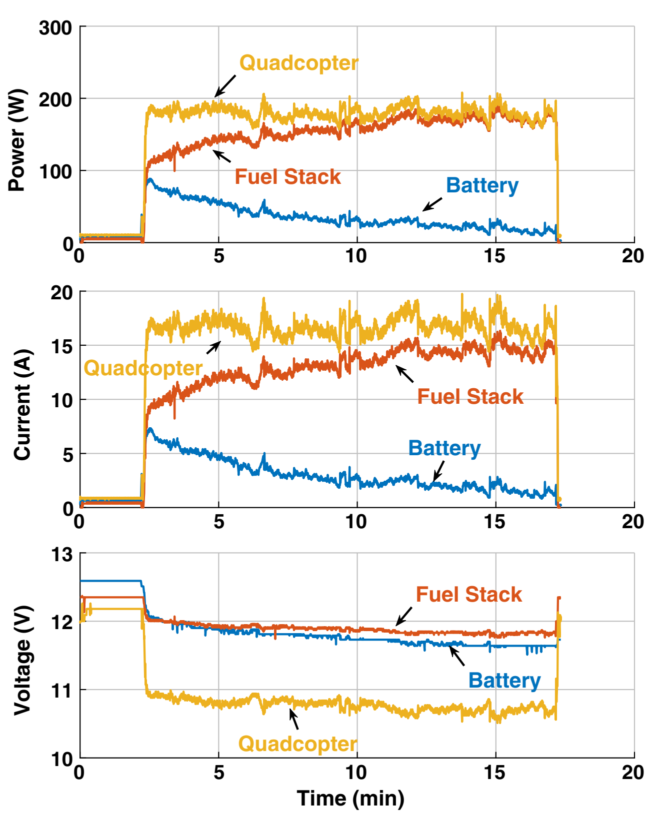

Fig. 9 Experimental power, current, and voltage of battery, fuel stack, and quadcopter during hover.

To implement the regulated power sharing architecture, a circuit was constructed based on a modification to a circuit in Ref. [9]. It is shown in Fig. 11. The fuel stack and battery are still connected in parallel with a diode to prevent current flow into the fuel stack. The additions to the unregulated circuit are the two switches to control charging or discharging of the battery and two dc–dc converters to assist with charging and discharging the battery. The switches are voltage controlled solid-state relays activated by an Arduino microcontroller. When the relay on the left is closed, the diode in that branch limits the current flow so that the battery can only discharge.

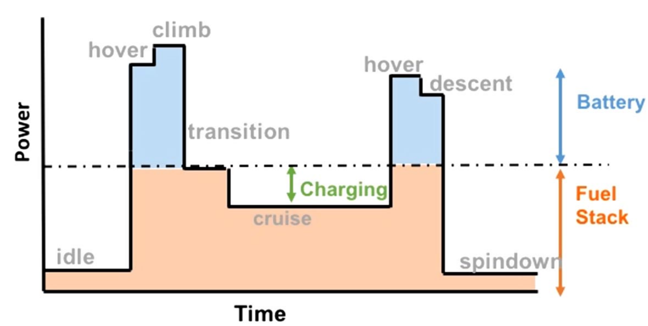

Fig. 10 Power supplied by fuel stack and battery in regulated operation for a notional mission power profile.

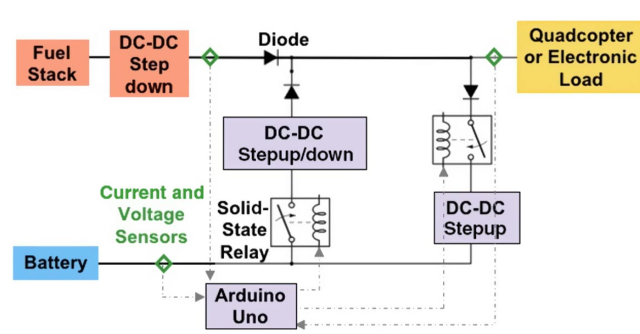

Fig. 11 Circuit schematic for regulated power sharing operation with added Arduino microcontroller, solid-state relay switches, and direct current (DC) converters.

When the relay on the right is closed instead, the diode in that branch channels the current flow in the direction to charge the battery. The stepup/-down (also called a buck/boost converter) in the battery charging branch (on the left) converts the battery voltage, which varies as a function of state of charge, to a constant voltage compatible with the output voltage of the fuel stack dc–dc stepdown. This voltage can be adjusted to provide a desired power sharing ratio between the fuel stack and battery during discharge. The stepup in the battery charging branch (on the right) outputs a constant current set by the designer, which allows for faster charging.

The Arduino sets the switches open or closed, depending on the battery voltage and load power. The various operating states are described in the following and listed in Table 5:

Table 5 Operating states of power sharing control circuit

State	Battery voltage	Load power	Switch states: Discharge	Switch states: Charge	Power source
1	Fully charged	Low	0	0	Fuel stack
2	Fully charged	High	1	0	Fuel stack + battery
3	Nominal	Low	0	1	Fuel stack + charge battery
4	Nominal	High	1	0	Fuel stack + battery
5	Fully depleted	Low	0	1	Fuel stack + charge battery
6	Fully depleted	High	0	0	Fuel stack
7	Current exceeding safe levels	— —	0	0	Fuel stack

1) For state 1, the battery is fully charged and the load power is low. All the power is supplied by the fuel stack, and the battery is completely disconnected from the circuit. Charging is not allowed to avoid overcharging the battery.

2) For state 2, the battery is fully charged and the load power is above that which can be supplied by the fuel stack alone. The battery discharge switch is closed, allowing the battery to share the load with the fuel stack.

3) For state 3, the battery is partially depleted but still above its safe minimum voltage. The load power is low. The battery is prevented from discharging because the fuel stack is capable of providing all the necessary power.

4) For state 4, the battery is in the same range as state 3 but the load power is above that which can be supplied by the fuel stack alone. The battery discharge switch is closed, allowing the battery to share the load with the fuel stack.

5) For state 5, the battery is completely depleted to its minimum safe voltage. The load power is low. The battery discharge switch is open, and so it cannot provide power to the load. The fuel stack provides all the power to the load and charges the battery if excess power is available.

6) For state 6, the battery is completely depleted but the load power is above the maximum fuel stack power. However, to prevent damaging the battery, it is still not allowed to discharge. If this case is ever reached, the battery was not sized adequately for the mission.

7) For state 7, if the battery charge or discharge current exceeds the maximum rated current, the switches open to disconnect it from the circuit as a safety precaution.

The first six states are demonstrated experimentally in Fig. 12. For this demonstration, the cutoff for a “high” or ”low” load was 20 W, and it is indicated by a dashed line in the power plots. This is an arbitrary number chosen for illustration purposes. The cutoff for high battery voltage was 12.3 V, and the cutoff for low battery voltage was 11.3 V. Both are plotted as dashed lines in the voltage plots. The Dchg and Chg lines indicate the time segments where the battery is discharging and charging, respectively. The boxes and numbers in the bottom plots indicate the corresponding states of operation. The setup used to obtain these data did not include the two dc–dc converters on the lower portion of Fig. 11.

When the fuel stack and battery are sharing power (cases 3 and 5), the sum of the fuel stack and battery currents equals the current received at the load. The sum of the fuel stack and battery power is

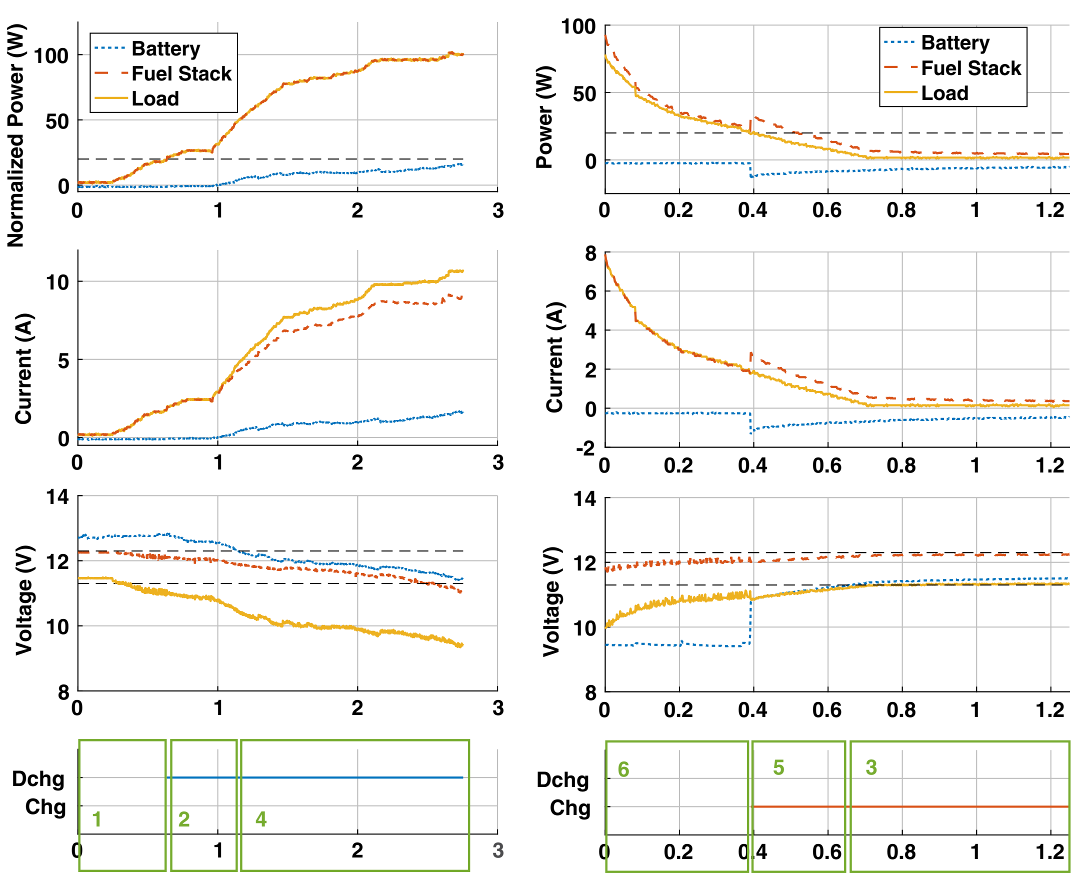

Fig. 12 Demonstration of power sharing circuit’s six operating modes.

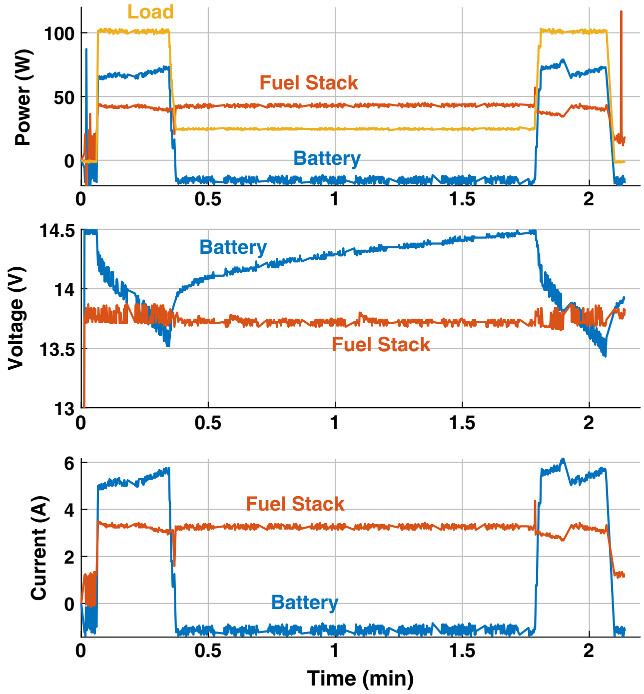

Fig. 13 Power, voltage, and current of battery and fuel stack in regulated parallel configuration; demonstrates ideal power sharing.

slightly greater than the power received by the load due to losses across the diodes and wires. The same is true for the other cases; the current is the conserved quantity and accurately illustrates the sharing of power, whereas the power is not conserved due to losses in the circuit. The illustration in Fig. 12 is open loop (no specific target ratio of power sharing), and hence does not require the dc–dc converters in the battery charging and discharging branches of Fig. 11.

The complete circuit with the dc–dc converters achieves control over power sharing and charging for a profile as seen in Fig. 10. A representative profile was placed on the circuit, and the results are shown in Fig. 13. This validates the ability of this circuit to achieve ideal power sharing where 1) the fuel stack operates at a constant power, 2) the battery supplements during high load portions of the mission, 3) a designer-defined constant ratio of battery and fuel stack power sharing is maintained, and 4) the fuel stack is used to charge the battery during low load portions (indicated by fuel stack power higher than load power and negative battery power). This minimizes the design power of the fuel stack and the design energy of the battery: both of which are principal driving factors for weight. Thus, to summarize, the concept to be used in the sizing section (Sec. VI) is demonstrated to be possible. The overhead incurred in weight and power is also reasonable.

V. Powerplant Weight

This section describes models to calculate fuel cell and battery system weights required for aircraft sizing. These weights depend on the operating characteristics (models of which were described earlier) desired from the powerplant. Also described are motor weights.

A. Motors

Several manufacturers have introduced ac permanent magnet synchronous motors for powering aircraft in the past few years. Reference [16] gave weights of 23 motors from six manufacturers (Thin Gap, Joby, EMRAX, YASA, Siemens, and UQM), of which 17 motors were designed for aeronautical applications. Several weight trends can be found in recent literature [13,17,36]. In this paper, only the 17 aeronautical motors are used. The weights follow torque with a maximum of ±30% error (see Ref. [16]):

$$W = 0.4025Q^{0.71} \tag{11}$$

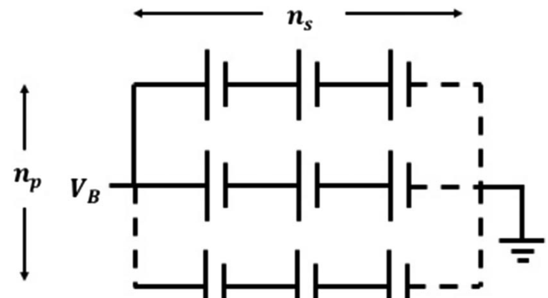

Fig. 14 Schematic of batteries or fuel cells connected in series and parallel.

where W is the mass in kilograms, and Q is torque in newtons per meter.

B. Lithium–Ion Batteries

The Li–ion battery model assumes n_s units in a series arranged in n_p cells in parallel (Fig. 14). The total number of cells is $n_p \times n_s$. The series–parallel arrangement allows for adding energy while keeping a desired voltage output. The cells are assumed to be identical. The battery voltage is $V_B = n_s v_c$. The current through each cell is i_c. The currents add, and so the battery current $I_B = n_p i_c$ or, equivalently, the battery capacity C_B (ampere hours) is related to the cell capacity C_c as $C_B = n_p C_c$. The energy capacity E_B (watt hours) is then

$$E_B = C_B V_B = n_p n_s C_c v_c = n_p n_s E_c$$

which is the total number of cells in the battery times the energy capacity of each cell. The battery weight is calculated from the weight of each cell.

For a known output voltage V_B, mission energy E_B, and a choice of cell C_c, the minimum weight is calculated as follows: The main equation is the cell weight versus capacity based on statistical fit of current-generation Li–ion cells. The data from eight suppliers to electric car manufacturers [*Automotive Energy Supply Corporation* (Nissan Leaf), LG Chem (Renault), Li-Tec (Daimler), Lithium Energy (Mitsubishi), Toshiba (Honda) and Panasonic (Tesla Model S)], shown in Fig. 15, follow the trend:

$$w_c = (0.0075 + 0.024C_c) \tag{12}$$

where w_c is in kilograms, and C_c is the capacity of a cell in ampere hours. So, the battery mass can be calculated as

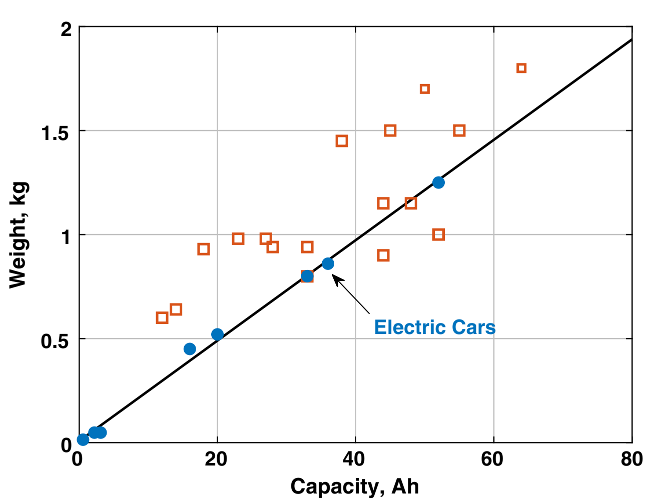

Fig. 15 Lithium–ion cell weights versus capacity in ampere hours.

$$
\begin{aligned}
& n_s = V_B/v_c \qquad (v_c = 3.7 \text{ V for Li ion}) \\
& C_B = P_B/V_B\zeta \quad \text{or} \quad E_B/v_B, \text{ (whichever is greater)} \\
& n_p = C_B/C_c \\
& w_c = (0.0075 + 0.024 C_c) f_T \qquad \text{(in kilograms)} \\
& W_B = w_c n_p n_s \qquad \text{(in kilograms)}
\end{aligned}
\tag{13}
$$

P_B (in watts) is the power, and ζ (h^{-1}) is the C rating. P_B/V_B is the current draw I_B. The minimum battery weight is found when I_B is the maximum (continuous, for the duration of P_B) discharge current. Then, $I_B = \zeta C_B$. If the C rate ζ is known, the required charge capacity C_B can be found.

Consider a segment of a mission where power P_B is required over time Δt. If the voltage is V_B, then the charge capacity needed for this segment will be $\Delta C_B = P_B \Delta t/V_B$. However, if the C rate is ζ, the power delivered can, at most, be $\zeta \Delta C_B V_B$. To ensure this equals P_B, the charge capacity must at least be $\Delta C_B = P_B/\zeta V_B$. Thus,

$$
\Delta C_B = \max\left(\frac{P_B \Delta t}{V_B}, \frac{P_B}{\zeta V_B}\right) \tag{14}
$$

where the first quantity is the capacity required to deliver the energy required, and the second is the capacity required to deliver the power required. If the second is greater, it means more energy is needed for the mission than necessary just to satisfy the power demand. The optimal condition is when both are the same:

$$
\zeta = 1/\Delta t \tag{15}
$$

For example, if high power is required only for 5 min (e.g., for hover), then $\zeta = 60/5 = 12\ \mathrm{h}^{-1}$. If a battery of this C rate (12 C) is not available, then more capacity must be carried on board than what is needed to deliver the energy. Typically, lithium–ion chemistries that store high energy have low C rates, and vice versa (2–4 C for 80–100 $(\mathrm{W \cdot h})/\mathrm{kg}$; and 0–1 C for 150–200 $(\mathrm{W \cdot h})/\mathrm{kg}$ at the battery pack level); thus, the total capacity must be evaluated carefully based on power segments and available C rates. In general, for constant power, P_B/ζ gives the energy in watt hours. For varying power, the energy is input from the mission, and ζ is found from the maximum power required. The numbers n_s and n_p are rounded to higher integers. The factor f_T is a technology factor; $f_T = 1$ places the specific energy at 150 $(\mathrm{W \cdot h})/\mathrm{kg}$, which represents a nominal state of the art at the battery pack level.

C. Proton Exchange Membrane Fuel Stack

Proton exchange (or electrolyte) membrane (PEM) fuel cells have lower specific power as compared to batteries (due to a heavy balance of plant) but can provide a dramatic increase in energy stored due to its hydrogen fuel. The degradation of its performance with low pressure is a problem in aeronautics, but not for on-demand air-taxi eVTOL, where the flight altitudes are expected to remain low. The problem of hydrogen storage and boiloff is also less significant in aviation as compared to cars, and it is lesser even for on-demand air-taxi eVTOL because of the shorter-duration missions and only a few hours of hydrogen storage (not weeks or months). Thus, the significant progress made in the past decade toward lighter gaseous hydrogen storage can be exploited to greater advantage.

A PEM fuel cell system consists of the stack and the hydrogen tank. For the stack, statistical weight models are difficult because of drastic variations based on cost (cell materials/catalyst), duty cycles (construction), and applications (household to cars to aircraft auxiliary power unit to UAVs). Specific powers can easily range from 0.1 kW/kg for inexpensive laboratory grade stacks to 2.0 kW/kg for expensive automobile stacks (see Ref. [16]).

A model suitable for design is one that is connected to stack geometry, materials, and operating characteristics so that improvements in constituent parts can flow into sizing. A simple model can be constructed as follows. Cells are assumed to be in series within a stack (which they typically are), similar to the arrangement of battery cells, to meet voltage and current requirements, shown in Fig. 14. Each cell is essentially a membrane electrode assembly (MEA). If the cross-sectional area is k_A times the active area A_c, the area density of each MEA ρ_c (in kilograms per square meter), thickness t_c (in meters), n_p cells in a stack, and an overhead fraction of η_O (to account for gaskets, seals, connectors, and endplates), then the weight W_{FS} and volume L_{FS} become

$$
W_{\mathrm{FS}} = \frac{k_A n_p A_c \rho_c}{1 - \eta_{\mathrm{OW}}}; \qquad L_{\mathrm{FS}} = \frac{k_A n_p A_c t_c}{1 - \eta_{\mathrm{OL}}}
$$

The maximum power output $P_{\max}$ is related to the maximum cell power density $p_{c\max}$ by $P_{\max} = p_{c\max} n_p A_c$. This can be rearranged: $n_p A_c = P_{\max}/p_{c\max}$. The fuel stack operation accessories contribute to a balance of plant power, and so a factor of f_{BOP} is added to increase the required maximum power output. Then, the weight model is

$$
W_{\mathrm{FS}} = \frac{k_A \rho_c}{1 - \eta_{\mathrm{OW}}} \frac{P_{\max}(1 + f_{\mathrm{BOP}})}{p_{c\max}} \tag{16}
$$

A value of $k_A = 4$ (conservative) is assumed in this paper. Published data from Honda [22] and Toyota [23,24] suggest $\rho_c = 1.57\mathrm{kg/m^2}$, $t_c = 0.001301$ m, and $\eta_{\mathrm{OW}} = 0.3$. The number of cells and the active area are found from the output voltage and power as $n_p = V/v_c$ and $A_c = P/(n_p p_c)$. The design cell voltage v_c (for maximum continuous power) is selected either to minimize the combined stack and tank weight or to ensure enough power margin (adequate maximum-rated power). The factor f_{BOP} is 20%, found in the Experimental Setup section (Sec. II), and it is a conservative value due to a low-end fuel stack and dc–dc stepdown.

The fuel flow rate, at any given power, is related to the cell voltage. Corresponding to $p_{c\max}$, a $v_{c\max}$ can be found from the cell $i - v$ characteristics. In general, at any power P, cell power density is $p = P/n_p A_c$; given p, the corresponding v can be found. The fuel flow rate is

$$
\dot{W}_F = \lambda_H \frac{m_H}{N_e F} \frac{P(1 + f_{\mathrm{BOP}})}{v} \tag{17}
$$

and the tank weight is

$$
W_{H2T} = \frac{1}{\eta_{\mathrm{BO}} w_{\mathrm{frac}}} \int \dot{W}_F \, \mathrm{d}t \tag{18}
$$

where λ_H is the effective stoichiometry (one for no loss in hydrogen utilization), $m_H = 2.016 \times 10^{-3}$ kg/mol is the molar mass, $N_e = 2$ is the number of electrons released by each hydrogen atom, $F = 96{,}485$ C/mole is Faraday's constant, P is the stack output power in watts, v is the operating cell voltage in volts, and η_{BO} is the boiloff efficiency factor. The effective stoichiometry is $\lambda_H = S_H \eta_H$, where S_H is the chemical stoichiometry (number of hydrogen molecules participating in reaction, here it is equal to 1) and η_H is the hydrogen utilization factor (typically 1–1.02). The tank weight W_{H2T} is found from the fuel weight W_F divided by the tank weight fraction w_f. For compressed hydrogen at 350 or 700 bar, the state of the art for long-duration storage is 5.5% ($w_f = 0.055$) (see Ref. [16]). Tolerating some hydrogen boiloff should allow greater weight fractions of 7.5–15% (for example, the UTC helicopter used 10%), or perhaps even 30%. The tank model is simply this weight fraction.

VI. eVTOL Sizing

Sizing involves calculating the minimum gross (total) takeoff weight W_{GTO} (in pounds) and engine power P_H (in horsepower) needed to carry a prescribed payload W_{PAY} (in pounds) over a prescribed mission. The major dimensions of the configuration [rotor (s) radius and solidity and wing(s) span and chord) fall out of sizing. If the maximum power is prescribed as an input, sizing involves calculating the maximum gross takeoff weight and payload.

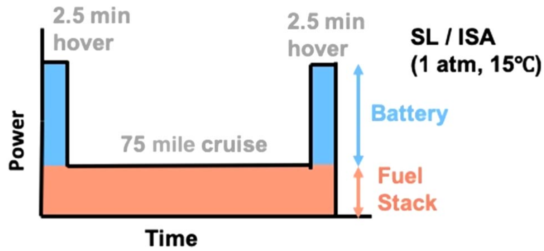

Fig. 16 Baseline power profile used in eVTOL sizing section (Sec. VI) showing B-FC hybrid power sharing scheme.

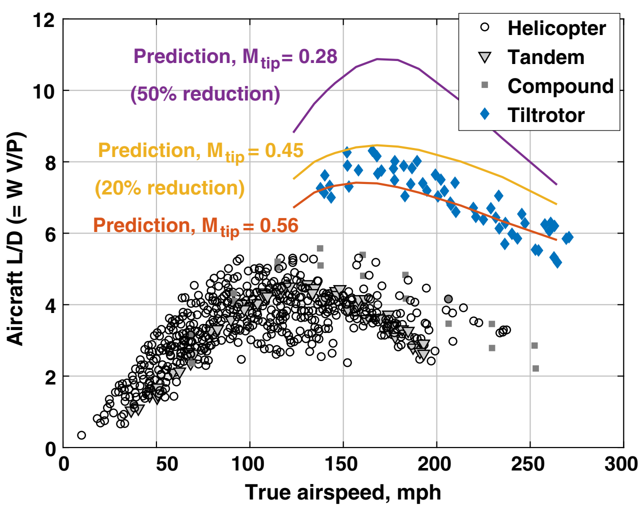

Fig. 17 ***L/D*** **versus true airspeed of VTOL aircraft; tiltrotor data from XV-15 in cruise mode (zero flaps, pylons down).**

An elementary mission is considered, which is representative of a simple on-demand intracity air-taxi operation (Fig. 16): only 5 min of hover (including reserves) and 75 miles of cruise range. The vehicle is sized for different powerplants: turboshaft, battery only, fuel cell only, and battery/fuel-cell hybrid. Battery charging from the fuel cell during flight is not considered.

The *Uber Elevate* paper [5] suggested a maximum hover power P_H of 500 kW (670 hp). This value is considered here. Three mission ranges are considered: a 75 mile baseline, a 150 mile extended range intercity mission, and a shorter 50 mile intracity mission. A total of 5 min of hover is included in each mission. Other attributes like cruise speed and gross weights influence the configuration, but they are outputs of the sizing process.

The lift-to-drag ratio L/D is shown for current vertical takeoff and landing (VTOL) aircraft in Fig. 17. The figure also shows analytical predictions of L/D for the XV-15 tiltrotor, based on a propulsive trim solution described later in this section. It includes predictions for a reduced tip speed, envisioned to be possible by using electric motors, which greatly improves rotor efficiency in cruise.

A. Sizing Methodology

The maximum power is prescribed as an input. Sizing calculates the maximum gross takeoff weight W_{GTO} and payload W_{PAY} for a range of disk loading (DL) $= W_{\mathrm{GTO}}/A$, where A is the total projected disk area of all lifting rotors.

The gross takeoff weight is the sum of the empty weight and the useful weight. The empty weight W_E is the structural weight W_S, the powerplant weight W_P, and a generic group of all other weights W_{Oth}. This group of all other weights refers to the weights of systems and equipment, including: electrical (on-board power supply, anti-icing), avionics, furnishings (seats, emergency equipment), and load and handling (vibration absorbers, contingency weights). In the absence of any available data, historical trends of helicopters are used (typically 30% of empty weight; $f_{\mathrm{WO}} = W_{\mathrm{Oth}}/W_E = 0.3$) [37]. The useful weight is the payload weight and fuel weight. The payload weight includes fixed useful weights, such as the pilot and crew, as well as any additional payload. These breakdowns are shown as follows:

$$\begin{aligned} W_{\mathrm{GTO}} &= W_E + W_{\mathrm{USE}} \\ W_E &= W_S + W_P + W_{\mathrm{Oth}} \\ W_{\mathrm{USE}} &= W_{\mathrm{PAY}} + W_{\mathrm{FUEL}} \end{aligned} \tag{19}$$

For each disk loading, the steps are as follows:

1) From the maximum engine power, calculate the maximum W_{GTO}. Typically, $P_{\mathrm{MAX}} = \mathrm{PFP}_H$, where PF is an installed power factor for excess power and P_H is from Eq. (20). Here, assume $\mathrm{PF} = 1$ for minimal hover capability:

$$P_H = \frac{1}{\mathrm{FM}} W_{\mathrm{GTO}} \sqrt{\frac{\mathrm{DL}}{2\rho}} \tag{20}$$

where ρ is density, and FM is the figure of merit (ideal induced power in hover divided by actual power), which is initialized as 0.6.

2) From disk loading and the number of rotors, find radius R. With R known, the FM can be updated. Here, the blade element theory is used, with uniform inflow, an induced power factor of $K_h = 0.07$, and XV-15 airfoil decks. The following are assumed: solidity of $\sigma = 0.1$, hover tip Mach number of $M_T = 0.55$, number of blades per rotor of $N_b = 3$, and international standard atmosphere (ISA)/sea level (SL) conditions (for density ρ and speed of sound c).

3) Calculate the power to cruise at speed V_C using Eq. (21):

$$P_C = \frac{WV_C}{L/D} \tag{21}$$

The aircraft weight W varies due to fuel burn (except for batteries), but the simple expression with $W = W_{\mathrm{GTO}}$ is appropriate for an initial estimate. The lift-to-drag ratio L/D is a function of cruise speed V_C, and this is where the configuration enters sizing.

The variation of L/D for a single edgewise rotor helicopter can be calculated using a standard momentum theory (with appropriate corrections). The aircraft drag area (in square feet) is estimated to be the minimum achieved by current helicopters (based on S-76, SA-341, and OH-6A helicopters as proposed by Harris [37]):

$$F = f_D \left(\frac{W_{\mathrm{GTO}}}{1000} \right)^{23}$$

where W_{GTO} is in lb and $f_D = 2.5$ for edgewise rotor helicopters (22)

The variation of L/D for a tiltrotor aircraft requires a more detailed analysis because of lift sharing between a wing and rotor(s) as well as a reduction of rotor speed in cruise, which affects aircraft pitch and rotor collective. A two-dimensional trim solution was developed, which balances forces in the horizontal x and vertical z directions. The forces are aircraft weight, aircraft drag, rotor lift, rotor propulsive force, wing lift, and wing drag. The trim variables are the aircraft pitch θ_{ac} and the rotor collective θ_{75}. This analysis results in L/D as a function of true airspeed, which is similar to that shown in Fig. 17 for the XV-15, but it is now calculated based on the aircraft parameters at a specific disk loading. For all disk loadings, the aircraft is assumed to be completely wingborne at 150 mph with a wing loading of 78 lb/ft^2 (XV-15 values). The wing aspect ratio is $AR = 6$ with an Oswald efficiency factor of $e = 0.8$. The wing airfoil is the VR-7 because the XV-15 wing airfoil is not available in the public domain. Component drags are scaled to gross takeoff weight based on XV-15 values given in Ref. [38].

The cruise speed for minimum P_C/V_C, which by definition is the speed for the best range V_{BR} (minimum energy spent per distance traveled), occurs at maximum L/D [Eq. (21)]. This speed is used for

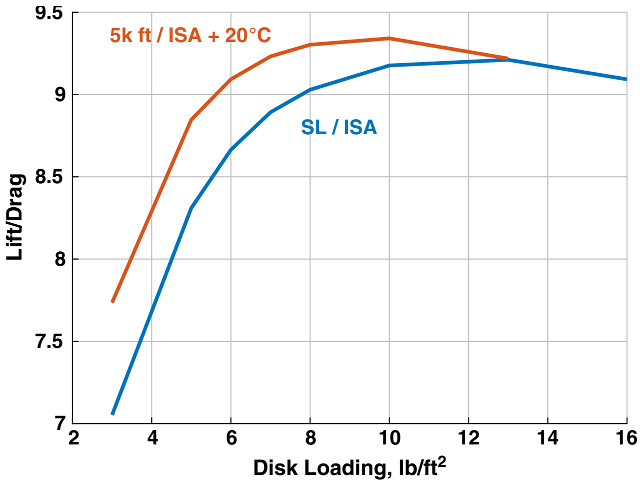

Fig. 18 Maximum lift-to-drag ratio versus disk loading for final aircraft designed for 75 mile range; at cruise tip Mach number of 0.28.

calculating cruise power. L/D versus DL for the final aircraft obtained in this process is shown in Fig. 18.

4) Calculate structural weight from statistical trends: $W_S = 0.24W_{\mathrm{GTO}}$ (state of the art for helicopters [37]), which is valid between 3000 and 100,000 lb gross takeoff weight rotorcraft. eVTOL aircraft are not guaranteed to follow this trend, but it can be considered a baseline target.

5) Calculate powerplant weight from weight models given earlier. Turboshaft:

$$W_P = 1.8\mathrm{HP}_H^{0.9}$$
$$\text{battery: } W_P = W_{\mathrm{motor}}$$
$$\text{fuelcell: } W_P = W_{\mathrm{motor}} \tag{23}$$

HP_H is the hover power in horsepower. The statistical trend for the turboshaft is valid between 300 and 20,000 engine horsepower. Any inefficiency due to electrical-to-mechanical conversion is neglected Calculate the fuel weight from the total energy required for the mission.

$$\text{Turboshaft:} W_{\mathrm{FUEL}} = \mathrm{SFC}E_{\mathrm{hp-h}}$$
$$\text{battery:} W_{\mathrm{FUEL}} = W_B$$
$$\text{fuelcell:} W_{\mathrm{FUEL}} = W_{H2T} + W_{\mathrm{FuelStack}}(1 + f_{\mathrm{OH}}) \tag{24}$$

$E_{\mathrm{hp-h}}$ is the mission energy in horsepower per hour. A specific fuel consumption (SFC) of 0.4 $\mathrm{lb}/(\mathrm{hp}\cdot\mathrm{h})$ is assumed. Note that f_{OH} is the 15% weight overhead associated with the fuel stack used in the experimental setup of this paper. Note that, although the fuel stack is not an expendable fuel mass, it is categorized as fuel weight to provide a fair comparison with the battery.

6) Calculate empty weight: $W_E = (W_P + W_S)/(1 - f_{\mathrm{WO}})$. The "all other" group is estimated as $W_{\mathrm{Oth}} = f_{\mathrm{WO}}W_E$, as described at the beginning of this section. Typically, this group constitutes up to 30% of W_E for modern aircraft, and so $f_{\mathrm{WO}} = 0.3$ [37].

7) Calculate useful load and payload:

$$W_{\mathrm{USE}} = W_{\mathrm{GTO}} - W_E$$
$$W_{\mathrm{PAY}} = W_{\mathrm{USE}} - W_{\mathrm{FUEL}}$$

and iterate steps 1–7 until the payload weight has converged.

B. Results of Sizing

The steps listed in the previous section were carried out for a notional mission of 5 min of hover at 500 kW and 75 miles of cruise at the best range speed at SL/ISA. This is an elementary mission appropriate for a new powerplant so that key trends do not get buried inside the details of startup, shutdown, reserves, etc. Additional weight needed for reserves and redundancy in batteries or fuel stacks is not considered. The purpose is to evaluate and compare the different powerplants.

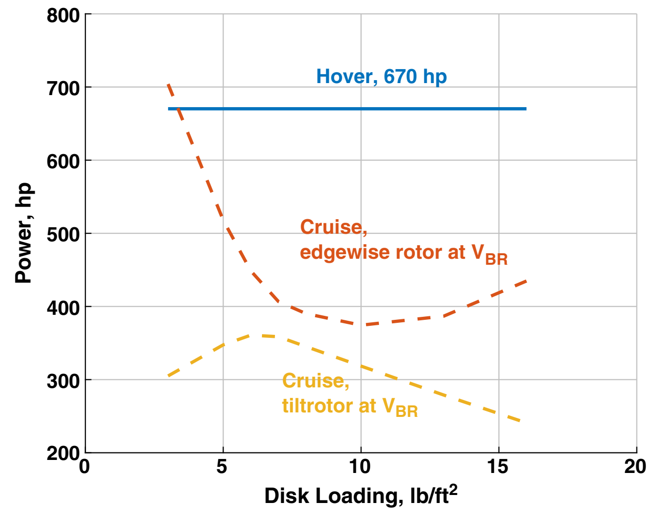

Fig. 19 Cruise power versus disk loading for edgewise and tilting proprotors.

The cruise powers for edgewise and tiltrotor configurations are shown in Fig. 19. For both the edgewise and tiltrotor configurations, the cruise speed is set to the best range speed V_{BR} at each disk loading. Tiltrotors require lower cruise power due to higher L/D. For the tiltrotor, the cruise power increases first, and then it drops with increasing DL; around 16 $\mathrm{lb}/\mathrm{ft}^2$, the cruise power is 240 hp. Edgewise rotors require significantly higher cruise power. At DL of 16, the cruise power is 430 hp. The minimum edgewise rotor cruise power occurs at 10 $\mathrm{lb}/\mathrm{ft}^2$ at 370 hp. The reduced cruise power has a dramatic impact on the feasibility of electric flight, and so only the tiltrotor configuration is considered henceforth for the electric powerplants.

Figures 20–25 show gross takeoff weights and payload weights for a variety of conceptual powerplants. Figure 20 shows the gross takeoff weights and payload weights for a turboshaft, fuel cell, battery, and B-FC hybrid powerplant. These sizing results are based on a two-rotor tiltrotor configuration. They use conservative baseline technology for electric power components. This includes a battery available specific energy of 150 $(\mathrm{W}\cdot\mathrm{h})/\mathrm{kg}$ (Saft, Tesla), a fuel cell specific power of 0.5 kW/kg (Toyota), and a hydrogen storage weight fraction of 5.4% (U.S. Department of Energy). The battery powerplant assumes that the battery is energy limited rather than

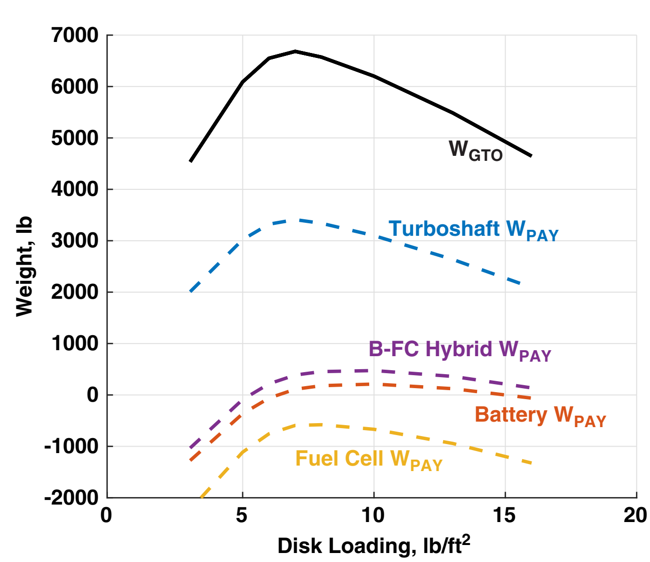

Fig. 20 Aircraft payload and gross take-off weights as a function of disk loading; various power sources; baseline technology; tilting proprotor configuration.

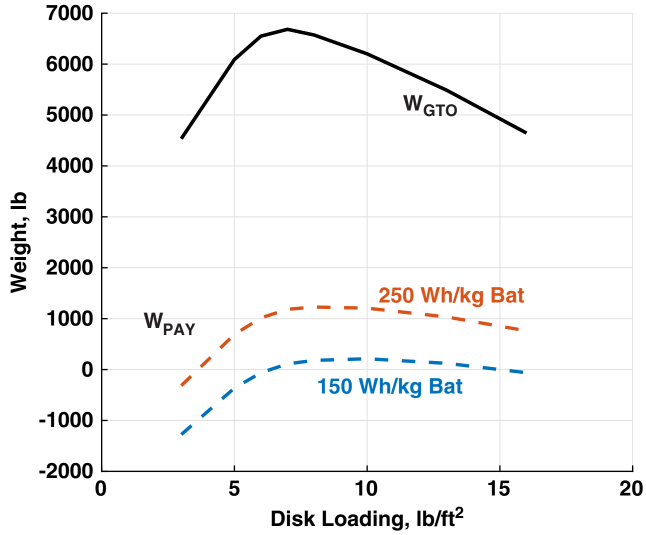

Fig. 21 Aircraft payload and gross take-off weights as a function of disk loading battery powered; improved technology; tilting proprotor.

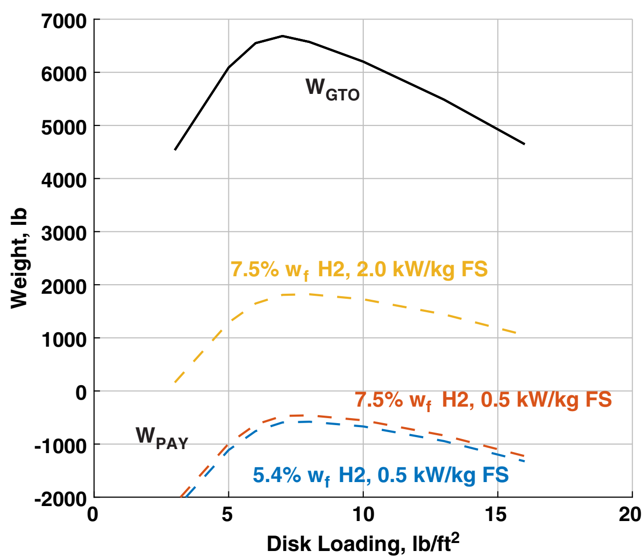

Fig. 22 Aircraft payload and gross take-off weights as a function of disk loading fuel cell powered; improved technology; tilting proprotor.

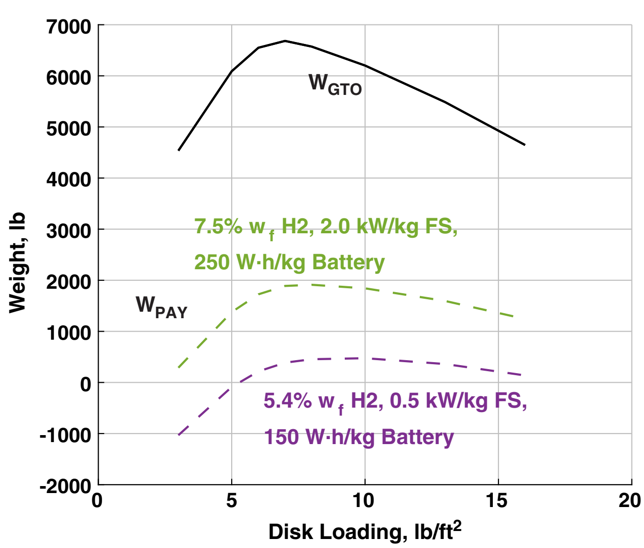

Fig. 23 Aircraft payload and gross take-off weights as a function of disk loading B-FC hybrid powered; baseline technology; tilting proprotor.

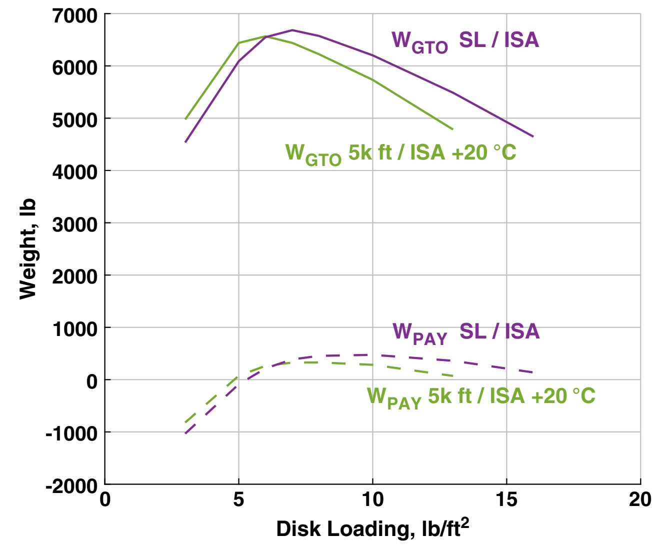

Fig. 24 Aircraft payload and gross take-off weights as a function of disk loading B-FC hybrid powered; high-altitude and -temperature comparison; baseline technology; tilting proprotor.

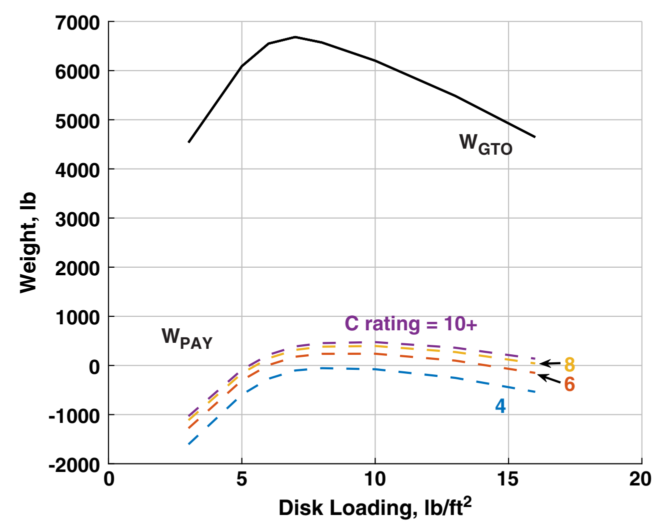

Fig. 25 Aircraft payload and gross take-off weights as a function of disk loading B-FC hybrid powered; baseline technology; tilting proprotor.

power limited, and it is therefore sized according to its specific energy. The C rate ζ is then a fallout. The hybrid powerplant includes a fuel stack sized to accommodate the prescribed cruise power, as well as a battery portion sized to accommodate the remaining energy for the mission. Charging the battery during the mission is not considered. The results show that, for this mission, only the B-FC hybrid powerplant can carry a payload. For a gross takeoff weight of 6200 lb, the payload weight is around 500 lb at a DL of 10 lb/ft^2. The weight breakdowns for this hybrid case at three different cruise ranges are shown in Table 6. The other cruise ranges are discussed in detail later. Fuel cells that provide 0.5 kW/kg specific power still require custom design. The batteries consist of 68 units of nine cells: each cell is rated at (10 C) 100 Ah. These are high-power cells and will require custom design.

Figure 21 shows the effects of an improvement in battery technology. It shows that, with a battery of 250 $(\text{W}\cdot\text{h})/\text{kg}$ available specific energy, a battery-only powerplant can accommodate a 1200 kg payload for a gross takeoff weight of 6200 lb. Figure 22 shows the effects of improvements in fuel cell and hydrogen storage technology. A 7.5% weight fraction is a reasonable value to use for aviation, where boiloff is of lesser concern than in automobiles. Increasing the specific power of a fuel stack to Toyota's reported 2 kW/kg decreases the weight of the powerplant significantly, to the point where a fuel cell powerplant can accommodate a useful payload

Table 6 Conceptual designs for a two-rotor tiltrotor aircraft for a 5 min hover mission (FS, fuel stack; H2, hydrogen; BAT, battery)

	Cruise range, miles			
	50	75	150	150
Powerplant type	Battery	Battery-FS	Battery-FS	Battery-FS, improved technology
W_{GTO}, lb	6572	6202	6202	6202
Disk loading, lb/ft^2	8	10	10	10
Rotor radius, ft	11.4	9.9	9.9	9.9
Maximum hover power, hp	670	670	670	670
Cruise power, hp	345	318	318	318
Cruise speed, mph	177	177	177	177
Total energy, hp·h	153	191	326	326
W_{PAY}, lb	834	475	84	1560
Fuel				
W_{FS}, lb	0	1257	1257	315
PEM (W·h)/kg	——	211	387	1544
PEM kW/kg	——	0.42	0.42	1.65
H2 kg	——	25	46	46
Tank w_f	——	5.4	5.4	5.4
W_B, lb	2058	396	396	243
BAT (W·h)/kg	152	152	152	248
BAT kW/kg	0.53	1.46	1.46	2.38
BAT current in C	3.5	9.6	9.6	9.6
Empty weight W_E				
W_P, lb	999	904	904	904
Motors, lb	714	646	646	646
Controller/inverter, lb	143	129	129	129
Cooling, lb	143	129	129	129
W_S, lb	1577	1488	1488	1488
W_{Oth}, lb	1104	1025	1025	1025

of around 1800 lb at a gross weight of 6600 lb. Figure 23 combines these improvements in a B-FC hybrid powerplant to achieve a payload of 1800 lb with a gross takeoff weight of 6200 lb, or a payload weight of 1900 lb for a gross takeoff weight of 6600 lb at a disk loading of 8 lb/ft^2. The greatest impact comes from increasing the fuel cell specific power to 2 kW/kg.

Figure 24 shows the effects of operating at increased altitude and temperature of 5000 ft and 20°C. This corresponds to an air density decrease from 0.00238 to 0.00194 slugs/ft^2 and a sound speed increase from 1116 to 1132 ft/s. As a result, the payload is reduced to 300 lb for a gross takeoff weight of 6200 lb.

Thus far, the powerplants involving batteries have been sized using specific energy, under the assumption that the specific power (or C rate) is not a limiting factor. Figure 25 shows how the payload weight changes if the battery is in fact power limited. A battery's specific power is based on its C rating, which specifies the maximum discharge current of the battery. The line for a C rating of 10+ in Fig. 25 is the same as the line in Fig. 20 for hybrid W_{PAY}, in which power was not a limiting factor. The other lines in Fig. 25 show a decreasing payload weight because the powerplant weight is increased by a larger battery requirement to provide sufficient power for the mission. A B-FC hybrid powerplant using a 6 C battery and baseline technology (150 (W · h)/kg battery, 0.5 kW/kg fuel cell, and 5% w_f tank) is only capable of carrying a payload of 200 lb.

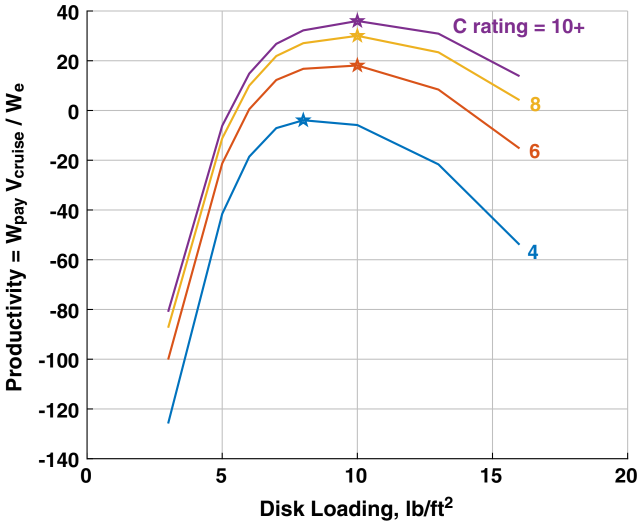

Fig. 26 Aircraft productivity as a function of disk loading B-FC hybrid powered; baseline technology; tilting proprotor.

Productivity is a metric used classically to select the optimal disk loading. Productivity is defined as the useful work done per dollar. Useful work is $W_{PAY} \times V_{cruise}$, and cost scales closely with W_E. The expression for productivity is $W_{PAY} \times V_{cruise}/W_E$. Figure 26 shows the productivity of the hybrid powerplant for different C ratings. Based on these results, the optimal eVTOL for this mission would have approximately a C rating of 10, disk loading of 10 lb/ft^2, W_{GTO} of 6200 lb, and a payload weight of 500 lb (based on Fig. 25).

The results have shown that a hybrid powerplant is necessary to achieve a 75 mile range with practical payload. To investigate the possibility of further extending the range, the same aircraft sizing was carried out for an extended mission of 150 mile of cruise. Figure 27 shows that, for this extended mission, only the B-FC hybrid powerplant is light enough to accommodate any payload at all. It achieves a payload weight of 100 lb for a gross takeoff weight of 6200 lb. Figure 28 shows the results if the improved technology factors are used (250 (W · h)/kg batteries, 7.5% w_f storage tanks, and 2.0 kW/kg fuel cells). With these numbers, the hybrid powerplant achieves a substantial payload of 1600 lb for a gross takeoff weight of 6200 lb. As in the previous mission, it is important to note that these results require a battery C rating of 10 C, as shown in Fig. 29. Note that, unlike in Fig. 25 for the 75 mile mission, this plot uses improved technology numbers. Even a 4 C battery can achieve a substantial payload of 1200 lb at a gross takeoff weight of 6200 lb. However, with baseline technology numbers, no payload is possible for a C rate below 10 C. The maximum productivity always occurs at a disk loading of 10 lb/ft^2, regardless of the battery C rate.

If the hover time were to decrease to less than 5 min, the C rating for the optimal powerplant would increase beyond 10 C. This is because the power required for hover remains the same, whereas the energy required is decreased. The battery is sized to meet the required energy, and so the battery weight required for a shorter hover mission will be smaller. However, because the power required is the same, for this smaller battery to deliver the same power, the C rating will increase.

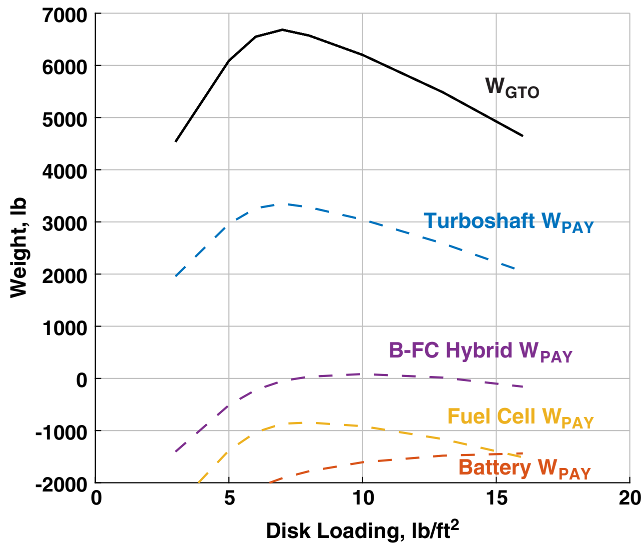

Fig. 27 Aircraft payload and gross take-off weights as a function of disk loading various power sources; baseline technology; tilting proprotor; extended range mission.

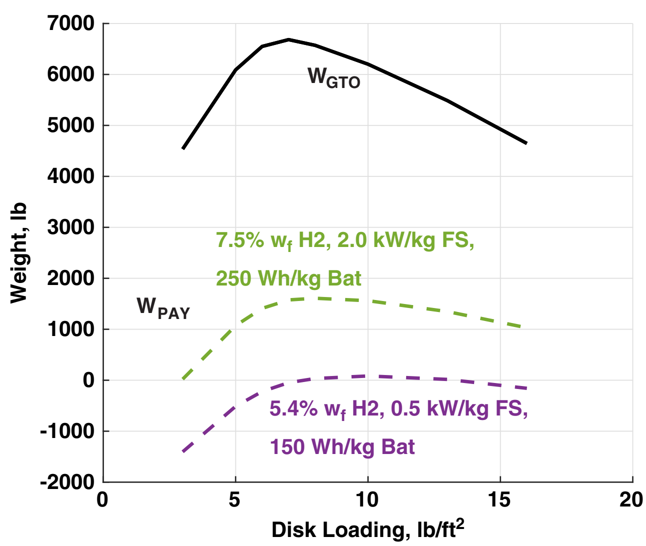

Fig. 28 Aircraft payload and gross take-off weights as a function of disk loading B-FC hybrid power; improved technology comparison; tilting proprotor; extended range mission.

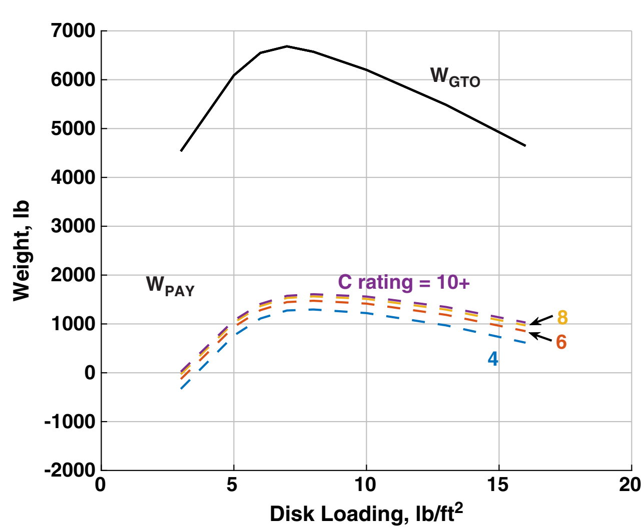

Fig. 29 Aircraft payload and gross take-off weights as a function of disk loading B-FC hybrid; improved technology; tilting proprotor; extended range mission.

The final mission is the shortest: 5 min hover and 50 mile cruise, which is perhaps barely sufficient for an intracity commute.

Figure 30 shows the W_{PAY} of different power configurations for a range of disk loadings. For this mission, the battery-only powerplant is best among the all-electric options. This is because less energy is required for the mission, and a relatively large portion of it is at high power, and so there is limited payoff for the high-energy hydrogen fuel. For a gross weight of 6200 lb, the battery-only system can carry a payload of 800 lb. Figure 31 shows how an improvement in battery specific energy to 250 $(\mathrm{W \cdot h})/\mathrm{kg}$ would increase the aircraft payload to 1600 lb. The fuel cell technology improvement results are identical to that of the baseline mission, shown in Fig. 22, because the fuel cell is sized to the maximum power, which remains the same for the abbreviated mission.

For the shortest mission, the battery-only configuration with baseline technology was chosen to investigate the effects of a limited C rating. The results are shown in Fig. 32. A C rating of at least 3 C is still needed for the battery powerplant, for a maximum payload of 500 lb, and an even greater C rating is needed for the hybrid.

Figure 33 shows the productivity of the battery-only power for various C ratings. Based on these results, the optimal aircraft for the shortest mission would be battery powered and would have,

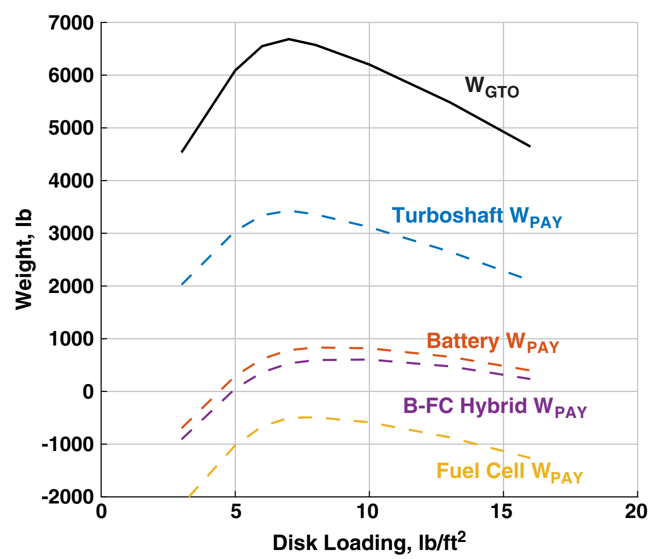

Fig. 30 Aircraft payload and gross take-off weights as a function of disk loading various powerplants; baseline technology; tilting proprotor; shortest intracity mission.

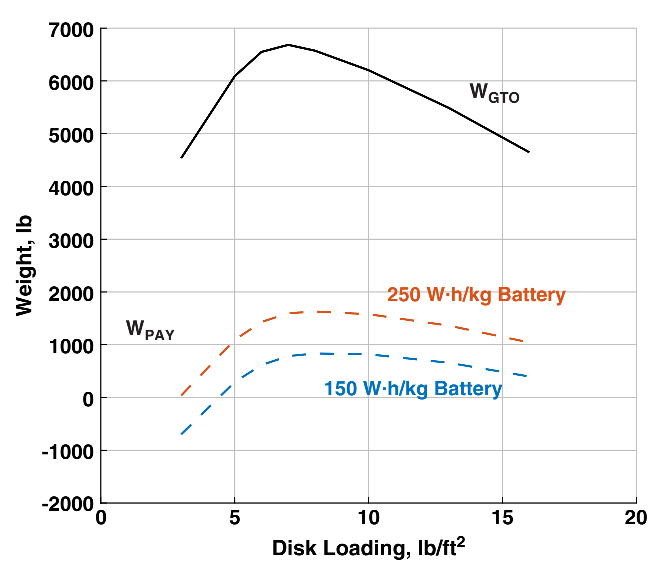

Fig. 31 Aircraft payload and gross take-off weights as a function of disk loading battery-only powerplant; improved technology comparison; tilting proprotor; shortest intracity mission.

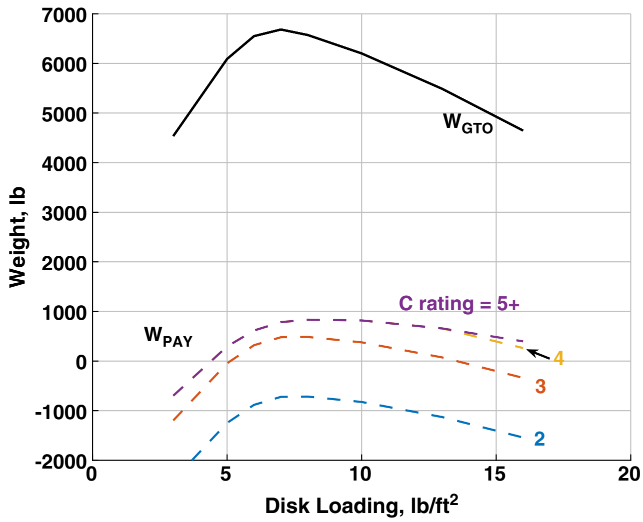

Fig. 32 Aircraft payload and gross take-off weights as a function of disk loading battery only; baseline technology; tilting proprotor; shortest intracity mission.

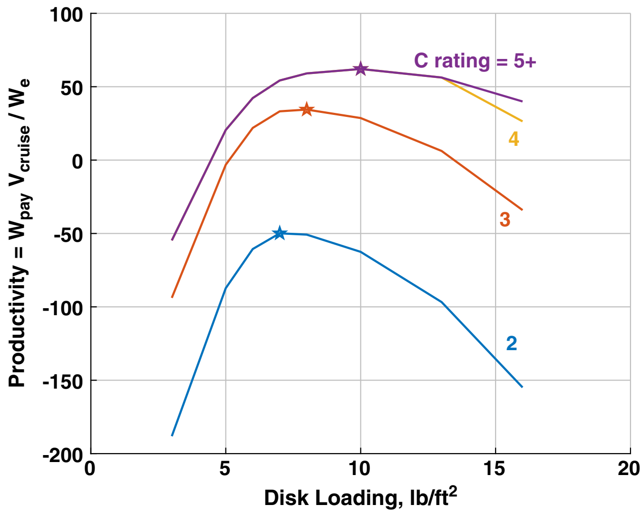

Fig. 33 Aircraft productivity as a function of disk loading fuel cell versus battery; baseline technology; limited battery C rating; tilting proprotor; shortest intracity mission.

approximately, batteries with a C rating of 4 C, a disk loading of 10 $\mathrm{lb/ft^2}$, W_{GTO} of 6200 lb, and a payload weight of 800 lb.

VII. Conclusions

The use of hydrogen fuel cells combined with Li–ion batteries was examined as a potential candidate to increase range, endurance, and payload of electric vertical takeoff and landing (eVTOL) aircraft. Based on systematic hardware testing, analytical modeling, and eVTOL sizing, the following key conclusions were drawn:

1) The transient nature of electrochemical sources is primarily driven by a first-order capacitative behavior. Battery and fuel cell transients can both be modeled using the same underlying equivalent circuit networks. The circuit elements, and consequently the time constants, are different. There are presently no first principle methods to identify these components easily, and so a semiempirical approach is essential.

2) The models developed in this paper were generally able to capture the magnitudes and waveforms of experimental data. Some mean errors existed for both the fuel stack and battery. Additionally, the fuel stack model failed to capture a transient occurring immediately after it was turned on, and the battery discharge rate model was less accurate when placed in parallel with a fuel stack for flight testing. In general, the voltage model was accurate to within 5% for both the battery and the fuel cell.

3) The fuel cells used in this research are in fact faster to respond than batteries, and both are agile enough to handle rapid power transients in vertical takeoff and landing, as long as the current remains in the nominal range. The time constant in the normal operating range for the fuel stack was 0.02 s; for the battery, it was 1.69 s. There are more significant transient behaviors in the low-current (high voltage) and high-current (low voltage) ranges that require further investigation. These limits are important for fuel cell eVTOL because they occur near the highest efficiency and highest-power limits of the fuel cell.

4) An estimate for the fuel stack balance of plant power losses was found to be 15–25% of operating power. This loss was primarily due to the dc–dc stepdown, a smaller additional loss associated with the diodes used for power sharing regulation, and a very small loss due to the length of electrical wiring.

5) An estimate for weight overhead of the fuel stack is 15%, which is again primarily from power electronics. This is the mass that would not be included in the reported specific power of a fuel stack. The value is conservative for this small low-end fuel stack and stepdown.

6) For a baseline mission of 75 miles using a tiltrotor aircraft, a fuel cell and battery combined powerplant is the best option. Using 150 $(\mathrm{W \cdot h})/\mathrm{kg}$ and 10 C batteries, a 0.5 $\mathrm{kW/kg}$ fuel stack, and a 5% w_f tank, an aircraft sized for this mission can carry 500 lb (at least two passengers) with a gross weight of 6200 lb and disk loading of 10 $\mathrm{lb/ft^2}$. The B-FC combination is superior to either electric power source alone.

7) For a longer intercity mission of 150 miles, the fuel cell and battery combined powerplant is the only option that gives a practical payload with present technology. At this range and speed, using baseline technology, a tiltrotor aircraft optimized for productivity (payload weight × speed/empty weight) has a disk loading of 10 $\mathrm{lb/ft^2}$, a gross weight of 6200 lb, and a payload of 100 lb.

8) For a short intracity mission of 50 miles, batteries alone are the lightest powerplant option. For this mission, using 4 C batteries with baseline energy density (150 $(\mathrm{W \cdot h})/\mathrm{kg}$), a 6200 lb aircraft with a disk loading of 10 $\mathrm{lb/ft^2}$ can carry 800 lb.

9) An improved battery C rate (i.e., power density) is critical to using batteries in eVTOL for practical payloads. Based on the mission profile used in this paper, with baseline numbers (150 $(\mathrm{W \cdot h})/\mathrm{kg}$ batteries, 0.5 $\mathrm{kW/kg}$ fuel stack, and 5% w_f tank), a 50 mile mission requires a 4 C battery for a payload of 800 lb or 3 C for a payload of 500 lb, a 75 mile mission requires 10 C for a payload of 500 lb or 6 C for a payload of 200 lb, and a 150 mile mission requires 10 C for a payload of 100 lb. The Current Battery Technology of 150 $(\mathrm{W \cdot h})/\mathrm{kg}$ and 3 C is insufficient to carry a practical payload for distances much more than 50 miles.

10) With future technology reported by the industry (250 $(\mathrm{W \cdot h})/\mathrm{kg}$ available for batteries, 2 $\mathrm{kW/kg}$ for fuel cells, and 7.5% w_f hydrogen storage) for the baseline mission of 75 miles, an aircraft with a gross takeoff weight of 6200 lb can carry a payload of 1900 lb with a B-FC hybrid powerplant, or 1800 lb with a fuel-cell-only powerplant. For the extended range of 150 miles, a 6200 lb aircraft can carry 1600 lb with a B-FC hybrid powerplant. For an intracity range of 50 miles, a 6200 lb aircraft can carry a 2000 lb payload using batteries alone.

11) Strategic investments for technology development depend on the target mission length. For missions longer than 50 miles, improved technology for fuel cell power density is very promising for combined battery and fuel cell powerplants. For shorter missions, improving battery energy density for battery powerplants is more important. For all mission lengths, battery power density must be improved to 4–10 C if specific energy remains limited to 150 $(\mathrm{W \cdot h})/\mathrm{kg}$ batteries.

Acknowledgments

This work is being carried out at the Alfred Gessow Rotorcraft Center, University of Maryland at College Park, under the Army/Navy/NASA Vertical Lift Research Center of Excellence (Award no. W911W61120012), with technical monitoring from Mahendra Bhagwat and William Lewis. Additional funding is provided by the U.S. Army Research Laboratory (Award no. W911NF1620155), with technical monitoring from Rajneesh Singh.

References

[1] Colucci, F., "Lift Where You Need It," *Vertiflite*, Vol. 62, No. 6, Nov.–Dec. 2016, pp. 26–30.

[2] Whittle, R., "Air Mobility Bonanza Beckons Electric VTOL Developers," *Vertiflite*, Vol. 63, No. 2, March–April 2017, pp. 14–21.

[3] Chretien, P., "The Quest for the World's First Electric Manned Helicopter Flight," *Vertiflite*, Vol. 58, No. 2, March–April 2012, pp. 38–42.

[4] Schneider, D., "Helicopters Go Electric," *IEEE Spectrum*, Vol. 49, No. 1, Jan. 2012, pp. 11–12. doi:10.1109/MSPEC.2012.6117817

[5] Holden, J., and Goel, N., "Fast-Forwarding to a Future of On-Demand Urban Air Transportation," *UBER Elevate*, Oct. 2016, pp. 1–97 .

[6] Lapeña-Rey, N., Mosquera, J., Bataller, E., and Ortí, F., "First Fuel-Cell Manned Aircraft," *Journal of Aircraft*, Vol. 47, No. 6, 2010, pp. 1825–1835. doi:10.2514/1.42234

[7] Rathke, P., Kallo, J., Schirmer, J., Stephan, T., Waiblinger, W., and Weiss-Ungethüm, J., "Antares DLR-H2 Flying Test Bed for Development of Aircraft Fuel Cell Systems," *ECS Transactions*, Vol. 51, No. 1, 2013, pp. 229–241. doi:10.1149/05101.0229ecst

[8] Flade, S., Kallo, J., Schirmer, J., and Stephan, T., "Comparison of Anode Configurations During Long Distance Flight in Fuel Cell Powered Aircraft Antares DLR-H2," *SciTech Forum 52nd Aerospace Sciences Meeting*, AIAA Paper 2014-0530, Jan 2014. doi:10.2514/6.2014-0530

[9] Kallo, J., Flade, S., Stephan, T., and Schirmer, J., "Antares DLR H2—Test Bed for Electric Propulsion," *53rd AIAA Aerospace Sciences Meeting*, AIAA Paper 2015-1305, Jan. 2015. doi:10.2514/6.2015-1305

[10] Romeo, G., Borello, F., Correa, G., and Cestino, E., "ENFICA-FC: Design of Transport Aircraft Powered by Fuel Cell & Flight Test of Zero Emission 2-Seater Aircraft Powered by Fuel Cells Fueled by Hydrogen," *International Journal of Hydrogen Energy*, Vol. 38, No. 1, 2013, pp. 469–479. doi:10.1016/j.ijhydene.2012.09.064

[11] Moffitt, B. A., and Zaffou, R., "Polymer-Electrolyte Fuel Cells for UAV Applications Providing Solutions to Revolutionize UAVs," *SAE 2012 Power Systems Conference*, Soc. of Automotive Engineers TP-2012-01-2161, Warrendale, PA, Oct. 2012. doi:10.4271/2012-01-2161

[12] "EnergyOr Shows off World's First Fuel Cell Multirotor UAV," *Fuel Cells Bulletin*, Vol. 2015, No. 4, April 2015, pp. 5–6. doi:10.1016/S1464-2859(15)30078-X

[13] Datta, A., and Johnson, W., "Requirements for a Hydrogen Powered All-Electric Manned Helicopter," *12th AIAA Aviation Technology, Integration, and Operations (ATIO) Conference and 14th AIAA/ISSMO Multidisciplinary Analysis and Optimization Conference*, AIAA Paper 2012-5405, 2012. doi:10.2514/6.2012-5405

[14] Datta, A., and Johnson, W., "Powerplant Design and Performance Analysis of a Manned All-Electric Helicopter," *Journal of Propulsion and Power*, Vol. 30, No. 2, Feb. 2014, pp. 490–505. doi:10.2514/1.B34843

[15] Ng, W., and Datta, A., "Development of Propulsion System Models for Electric-VTOL Aircraft," *2018 AIAA Aerospace Sciences Meeting, AIAA SciTech Forum*, AIAA Paper 2018-1750, Jan. 2018. doi:10.2514/6.2018-1750

[16] Ng, W., and Datta, A., "An Examination of Hydrogen Fuel Cells and Lithium-Ion Batteries for Electric Vertical Take-Off and Landing (eVTOL) Aircraft," *44th European Rotorcraft Forum*, Delft, The Netherlands, Sept. 2018, Paper 113.

[17] Sinsay, J. D., Alonso, J. J., Kontinos, D. A., Melton, J. E., and Grabbe, S., "Air Vehicle Design and Technology Considerations for an Electric VTOL Metro-Regional Public Transportation System," *12th AIAA ATIO Conference*, AIAA Paper 2012-5404, 2012. doi:10.2514/6.2012-5404

[18] Nagaraj, V. T., and Chopra, I., "Explorations of Novel Powerplant Architectures for Hybrid Electric Helicopters," *Proceedings of the 70th Annual Forum of the American Helicopter Society*, Montreal, May 2014.

[19] Snyder, C. A., "Exploring Propulsion System Requirements for More and All-Electric Helicopters," *22nd International Symposium on Air Breathing Engines (ISABE)*, Paper 2015-20221, Phoenix, AZ, 2015.

[20] Dever, T. P., Duffy, K. P., Provenza, A. J., Loyselle, P. L., Choi, B. B., Morrison, C., and Lowe, A., "Assessment of Technologies for Noncryogenic Hybrid Electric Propulsion," NASA TP-2015-21658, 2015.

[21] Johnson, W., "NDARC NASA Design and Analysis of Rotorcraft," NASA TP-2015-218751, 2016.

[22] Matsunaga, M., Fukushima, T., and Ojima, K., "Powertrain System of Honda FCX Clarity Fuel Cell Vehicle," *World Electric Vehicle Journal*, Vol. 3, No. 4, 2009, pp. 820–829. doi:10.3390/wevj3040820

[23] Hasegawa, T., Imanishi, H., Nada, M., and Ikogi, Y., "Development of the Fuel Cell System in the Mirai FCV," *SAE 2016 World Congress and Exhibition*, Soc. of Automotive Engineers TP-2016-01-1185, Warrendale, PA, 2016. doi:10.4271/2016-01-1185

[24] Yoshida, T., and Kojima, K., "Toyota MIRAI Fuel Cell Vehicle and Progress Toward a Future Hydrogen Society," *Electrochemical Society Interface*, Vol. 24, No. 2, 2015, pp. 45–49. doi:10.1149/2.F03152if

[25] O'Hayre, R., Cha, S., Colella, W., and Prinz, F. B., *Fuel Cell Fundamentals*, 2nd ed., Wiley, Hoboken, NJ, 2009. doi:10.1002/9781119191766

[26] Yan, Q., Toghiani, H., and Causey, H., "Steady State and Dynamic Performance of Proton Exchange Membrane Fuel Cells (PEMFCs) Under Various Operating Conditions and Load Changes," *Journal of Power Sources*, Vol. 161, No. 1, 2006, pp. 492–502. doi:10.1016/j.jpowsour.2006.03.077

[27] Yan, Q., Toghiani, H., and Wu, J., "Investigation of Water Transport Through Membrane in a PEM Fuel Cell by Water Balance Experiments," *Journal of Power Sources*, Vol. 158, No. 1, 2006, pp. 316–325. doi:10.1016/j.jpowsour.2005.09.013

[28] Amphlett, J. C., Mann, R. F., Peppley, B. A., Roberge, P. R., and Rodrigues, A., "A Model Predicting Transient Responses of Proton Exchange Membrane Fuel Cells," *Journal of Power Sources*, Vol. 61, Nos. 1–2, July–Aug. 1996, pp. 183–188. doi:10.1016/S0378-7753(96)02360-9

[29] Ceraolo, M., Miulli, C., and Pozio, A., "Modelling Static and Dynamic Behavior of Proton Exchange Membrane Fuel Cells on the Basis of Electro-Chemical Description," *Journal of Power Sources*, Vol. 113, No. 1, Jan. 2003, pp. 131–144. doi:10.1016/S0378-7753(02)00565-7

[30] Benziger, J., Chia, E., Moxley, J. F., and Kevrekidis, I. G., "The Dynamic Response of PEM Fuel Cells to Changes in Load," *Chemical Engineering Science*, Vol. 60, No. 6, March 2005, pp. 1743–1759. doi:10.1016/j.ces.2004.10.033

[31] Ziogou, C., Voutetakis, S., Papadopoulou, S., and Georgiadis, M. C., "Modeling, Simulation and Experimental Validation of a PEM Fuel Cell System," *Computers and Chemical Engineering*, Vol. 35, No. 9, Sept. 2011, pp. 1886–1900. doi:10.1016/j.compchemeng.2011.03.013

[32] Gao, L., Liu, S., and Dougal, R. A., "Dynamic Lithium-Ion Battery Model for System Simulation," *IEEE Transactions on Components and Packaging Technologies*, Vol. 25, No. 3, Sept. 2002, pp. 495–505. doi:10.1109/TCAPT.2002.803653

[33] Shepherd, C. M., "Design of Primary and Secondary Cells II. An Equation Describing Battery Discharge," *Journal of the Electrochemical Society*, Vol. 112, No. 7, 1965, pp. 657–664. doi:10.1149/1.2423659

[34] Dong, T. K., Kirchev, A., Mattera, F., Kowal, J., and Bultel, Y., "Dynamic Modeling of Li-Ion Batteries Using an Equivalent Electrical Circuit," *Journal of the Electrochemical Society*, Vol. 158, No. 3, Jan. 2011, pp. A326–A336. doi:10.1149/1.3543710

[35] Markel, T., Brooker, A., Hendricks, T., Johnson, V., Kelly, K., Kramer, B., O'Keefe, M., Sprik, S., and Wipke, K., "ADVISOR: A Systems Analysis Tool for Advanced Vehicle Modeling," *Journal of Power Sources*, Vol. 110, No. 2, Aug. 2002, pp. 255–266. doi:10.1016/S0378-7753(02)00189-1

[36] McDonald, R. A., "Electric Propulsion Modeling for Conceptual Aircraft Design," *52nd Aerospace Sciences Meeting, AIAA SciTech Forum*, AIAA Paper 2014-0536, Jan. 2014. doi:10.2514/6.2014-0536

[37] Harris, F. D., "Introduction to Autogyros, Helicopters, and Other V/STOL Aircraft, Vol. II: Helicopters," NASA SP-2012-215959, 2012.

[38] Johnson, W., "NDARC—NASA Design and Analysis of Rotorcraft Validation and Demonstration," *Proceedings of the AHS Aeromechanics Specialists Conference*, San Francisco, CA, Jan. 2010.